Title

Quantification of microenvironmental metabolites in murine cancer models reveals determinants of tumor nutrient availability

Running Title

Quantification of tumor nutrient availability

Impact Statement

Nutrient availability is an important tumor microenvironmental factor that impacts cancer cell biology; we developed methods to measure nutrients available to tumor cells and characterized factors that influence tumor nutrient availability.

Authors

Mark R. Sullivan[1], Laura V. Danai[1,2], Caroline A. Lewis[3], Sze Ham Chan[3], Dan Y. Gui[1], Tenzin Kunchok[3], Emily A. Dennstedt[1], Matthew G. Vander Heiden[1,4#] and Alexander Muir[1,5#]

[1]Koch Institute for Integrative Cancer Research and Department of Biology, Massachusetts Institute of Technology, Cambridge, MA 02139, USA; [2]Department of Biochemistry and Molecular Biology, University of Massachusetts, Amherst, Amherst, MA 01003, USA; [3]Department of Biology and Whitehead Institute for Biomedical Research and Massachusetts Institute of Technology, Cambridge, MA 02142, USA; [4]Dana-Farber Cancer Institute, Boston, MA 02115, USA; [5]Ben May Department for Cancer Research, University of Chicago, Chicago, IL 60637, USA

[#]Correspondence: amuir@uchicago.edu or mvh@mit.edu

Abstract

Cancer cell metabolism is heavily influenced by microenvironmental factors, including nutrient availability. Therefore, knowledge of microenvironmental nutrient levels is essential to understand tumor metabolism. To measure the extracellular nutrient levels available to tumors, we developed a quantitative metabolomics method to measure the absolute concentrations of >118 metabolites in plasma and tumor interstitial fluid, the extracellular fluid that perfuses tumors. Comparison of nutrient levels in tumor interstitial fluid and plasma revealed that the nutrients available to tumors differ from those present in circulation. Further, by comparing interstitial fluid nutrient levels between autochthonous and transplant models of murine pancreatic and lung adenocarcinoma, we found that tumor type, anatomical location and animal diet affect local nutrient availability. These data provide a comprehensive characterization of the

41 nutrients present in the tumor microenvironment of widely used models of lung and pancreatic
42 cancer and identify factors that influence metabolite levels in tumors.
43
44 **Introduction**
45
46 Tumors exhibit altered metabolism compared to non-transformed tissues (DeBerardinis
47 and Chandel, 2016). For example, animal limbs transformed with oncogenic viruses exhibit
48 increased glucose uptake and lactate secretion relative to unaffected limbs (Cori and Cori,
49 1925). Some aspects of tumor metabolism, including higher rates of glucose fermentation to
50 lactate, are cell-intrinsic features that are retained when cancer cells are isolated from tumors
51 (Koppenol et al., 2011). Indeed, numerous studies have delineated how cell-intrinsic factors
52 such as oncogenic genetic lesions or epigenetic state alter cellular metabolism, causing
53 phenotypes such as increased glycolysis (Nagarajan et al., 2016).
54 However, beyond cell-intrinsic alterations, tumors have modified tissue architecture and
55 an altered tissue microenvironment; these cell-extrinsic factors can also impact the metabolism
56 of tumors (Muir et al., 2018). For instance, the metabolic utilization of both glucose and the
57 amino acid glutamine differs between cells growing in culture and murine tumor models.
58 (Davidson et al., 2016; Muir et al., 2017; Sellers et al., 2015; Tardito et al., 2015). Further, the
59 metabolic enzymes that cancer cells rely upon for proliferation in culture are different than those
60 that the same cells utilize to support growth and survival in tumors (Alvarez et al., 2017;
61 Possemato et al., 2011; Yau et al., 2017). Thus, cancer cell metabolism is influenced by
62 microenvironmental cues.
63 Numerous microenvironmental factors affect cancer cell metabolism (Anastasiou, 2017;
64 Bi et al., 2018; Muir et al., 2018; Wolpaw and Dang, 2018), including the presence of stromal
65 cells (Lyssiotis and Kimmelman, 2017; Morandi et al., 2016), tumor acidity (Corbet and Feron,
66 2017; Persi et al., 2018), extracellular matrix properties (DelNero et al., 2018; Tung et al., 2015)
67 and tumor nutrient levels (Muir and Vander Heiden, 2018). In particular, environmental nutrient

68 availability is an important regulator of cancer cell metabolism (Cantor et al., 2017; Muir et al.,
69 2017; Schug et al., 2015; Tardito et al., 2015). Nutrient differences between standard cell
70 culture and animal tumor models can drive substantial changes in cancer cell metabolism that
71 alter the response of cancer cells to metabolically targeted drugs (Cantor et al., 2017; Gui et al.,
72 2016; Muir et al., 2017; Palm et al., 2015), such that drugs that inhibit proliferation of cancer
73 cells in culture fail to exhibit efficacy in tumors derived from the same cells (Biancur et al., 2017;
74 Davidson et al., 2016). Thus, determining the concentrations of nutrients in the tumor
75 microenvironment is important to understand and therapeutically target cancer cell metabolism.
76 Tumors and tissues are supplied with nutrients through the vasculature, which filters a
77 nutrient rich fluid from the circulation into the interstitial space of a tissue or tumor (Wiig and
78 Swartz, 2012). The interstitial fluid (IF) then perfuses through the tissue or tumor, exchanging
79 nutrients and wastes with cells. IF is then drained from the tissue or tumor via capillaries and the
80 lymphatic system. Thus, cells in tissues or tumors are not necessarily directly exposed to the
81 nutrients in circulating plasma, but instead are exposed to IF nutrient levels. For healthy organs,
82 IF nutrient levels may be similar to circulating nutrient levels, as these tissues are well
83 vascularized, allowing rapid metabolic exchange with the plasma. Indeed, the IF glucose
84 concentration in healthy skin is very similar to that of circulating plasma (Lonnroth et al., 1987).
85 In contrast to the functional vessels found in normal tissues, tumors commonly have an
86 abnormal vasculature with few vessels transporting blood (Fukumura et al., 2010). This may
87 lead to reduced nutrient delivery and waste exchange between tumor cells and the circulation.
88 Thus, tumor interstitial fluid (TIF) is thought to be nutrient depleted and have increased
89 concentrations of metabolic waste products. Indeed glucose levels in the TIF of some tumors
90 are lower than in the circulation, while lactate levels are higher (Burgess and Sylven, 1962;
91 Gullino et al., 1964; Ho et al., 2015). However, despite the importance of nutrient availability in
92 regulating tumor metabolism and drug sensitivity, TIF nutrients beyond glucose and lactate have

93 not been comprehensively measured, and the factors that determine TIF composition have not
94 been characterized.
95 We sought to systematically measure absolute nutrient concentrations in plasma and
96 TIF. To do so, we have developed a quantitative mass spectrometry-based approach using both
97 external standards and stable isotope dilution of a library of carbon labeled metabolites allowing
98 for quantification of >118 nutrients in any biofluid. We applied this technique to measure nutrient
99 levels in plasma and TIF isolated from autochthonous and transplantation models of murine
100 lung (LUAD) and pancreatic adenocarcinomas (PDAC) driven by activation of Kras and deletion
101 of p53. Interestingly, we found that anatomical location and tumor tissue of origin are both major
102 determinants of TIF nutrient composition. Dietary changes are also reflected in TIF nutrient
103 levels, while introduction of a *Keap1* mutation into LUAD cells had a smaller effect on the
104 composition of the metabolic tumor microenvironment. Collectively, these experiments elucidate
105 the microenvironmental constraints placed upon tumor metabolism by TIF nutrient levels and
106 provide insight into the factors that dictate tumor nutrient availability.
107
108 **Results**
109 ***Isolation of TIF from murine PDAC tumors***
110 We first focused on isolating and analyzing TIF nutrient levels in pancreatic ductal
111 adenocarcinoma (PDAC), as this tumor type is known to have inadequate vasculature leading to
112 tumor hypoxia (Koong et al., 2000) and nutrient deprivation (Commisso et al., 2013; Kamphorst
113 et al., 2015; Lyssiotis and Kimmelman, 2017; Sherman et al., 2017; Sousa et al., 2016). End-
114 stage tumors were isolated from the *LSL-Kras*$^{G12D/+}$*; Trp53*$^{flox/flox}$*; Pdx-1-Cre*, (KP-/-C) mouse
115 model of PDAC (Bardeesy et al., 2006). This mouse model recapitulates many aspects of the
116 human disease including dense stroma (Bardeesy et al., 2006) and alterations in systemic
117 metabolism (Danai et al., 2018; Mayers et al., 2014). We applied a previously described method
118 to collect TIF; tumors were placed on a fine mesh and subjected to low speed centrifugation

119 (Figure 1A) (Haslene-Hox et al., 2011). The mesh prevents cells from passing through but
120 allows TIF to flow out of the tumor and into a collection tube. This method has previously been
121 successfully used to study glucose and lactate levels in tumor samples (Ho et al., 2015; Siska et
122 al., 2017). 5-30 μL of TIF was able to be isolated from ~75% (13/17 tumors) of isolated KP-/-C
123 PDAC tumors. The remaining 25% of tumors did not yield any fluid. The amount of fluid
124 collected per tumor weight is consistent with previous reports of TIF isolation from human tumor
125 samples (Haslene-Hox et al., 2011).
126 Critically, this centrifugation method does not cause lysis of cells when performed on
127 human tumor samples, ensuring that the isolated fluid is interstitial and not intracellular fluid
128 (Haslene-Hox et al., 2011). To determine the extent to which intracellular fluid from lysed cells
129 might contribute to TIF isolated from the KP-/-C PDAC mouse model, we measured the level of
130 activity of the intracellular enzyme lactate dehydrogenase (LDH) in plasma and TIF from mice
131 bearing PDAC tumors (Figure 1B). As LDH is an intracellular enzyme, LDH activity should
132 indicate the extent to which intracellular material is present in the isolated interstitial fluid. The
133 level of LDH activity in the entire volume of collected TIF was less than 1% of that detected in
134 the whole lysed tumor (Figure 1B), suggesting that intracellular fluid is not a major component of
135 TIF isolated using this method. Though levels of LDH activity in the PDAC TIF samples were
136 ~20 fold higher than those found in plasma samples, similar or higher LDH activities were
137 recovered in TIF of solid tumors isolated by orthogonal methods (~60-80 fold higher LDH
138 activity in TIF than plasma) (Burgess and Sylven, 1962). These data suggest that TIF isolation
139 by centrifugation does not result in gross cell lysis and contamination of interstitial fluid with
140 intracellular material.
141
142 ***Quantification of TIF metabolites***
143 In order to understand the composition of the tumor microenvironment, we sought to
144 measure the absolute concentrations of metabolites present in TIF using liquid

145 chromatography/mass spectrometry (LC/MS). Absolute LC/MS quantification of metabolites in
146 biological samples such as plasma and TIF is complicated by matrix effects, which alter the
147 ionization and detection of metabolites in different sample types (Trufelli et al., 2011). Indeed,
148 when the same amounts of ^{13}C stable isotope labeled metabolites were added to water or
149 mouse plasma, detected levels of these ^{13}C standards varied widely depending on whether the
150 metabolites were dissolved in water or plasma (Figure 1C). This result reaffirms the presence of
151 significant matrix effects that would confound the comparison of metabolite concentrations
152 measured in different sample types. As a result, the use of external standard curves of
153 metabolites suspended in water can result in systematic error when used to quantitate
154 metabolites in complex mixtures such as plasma and TIF. To circumvent this problem, we
155 utilized stable isotope dilution quantification, in which ^{13}C stable isotope labeled metabolites are
156 added to each biological sample in known quantities, and the ratio of $^{12}C/^{13}C$ for each metabolite
157 is used to calculate the concentration of the ^{12}C metabolite (Figure 1D). As both ^{12}C and ^{13}C
158 metabolites are subject to the same sample-dependent ion enhancement or suppression
159 effects, this method limits error from matrix effects in metabolite quantification (Trufelli et al.,
160 2011).

161 To quantitate many metabolites simultaneously using the stable isotope dilution method,
162 we utilized a metabolite extract derived from yeast grown on a ^{13}C carbon substrate in which
163 intracellular metabolites are exhaustively labeled with ^{13}C. Such libraries have been shown to
164 improve the accuracy and precision in metabolite measurements in biological fluids such as
165 plasma (Hermann et al., 2018). In order to use metabolites in the ^{13}C yeast extract as
166 quantitative internal standards, we first quantitated the labeled metabolites in the ^{13}C yeast
167 extract by comparison with external standard curves of 149 polar metabolites detected in
168 previous studies of human plasma metabolite levels (Cantor et al., 2017; Evans et al., 2009;
169 Lawton et al., 2008; Mazzone et al., 2016). 70 metabolites from TIF and plasma samples were
170 quantified by stable isotope dilution using the ^{13}C yeast extract (Supplementary File 1), with

171 lower limits of detection ranging from 100nM to 3μM (Supplementary File 1). The remaining 79
172 metabolites were not detected in the ^{13}C yeast extract. These metabolites were instead
173 quantified in the TIF and plasma samples by fitting metabolite peak intensity in the samples to
174 the external standard curves (external standard calibration) (Supplementary File 1). These
175 measurements are subject to matrix effects of unknown magnitude. We measured the inter-day
176 reproducibility of our method for quantifying metabolites using both stable isotope dilution and
177 calibration to external standard curves in 6 PDAC TIF samples (Figure 1 – figure supplement 1).
178 There was a high degree of correlation across 5 orders of magnitude of metabolite
179 concentrations measured in the TIF samples analyzed by either stable isotope dilution or by
180 calibration to external standards on separate days. Our degree of reproducibility is similar to
181 other quantitative metabolomics studies (Chen et al., 2016). However, particularly for low
182 abundance metabolites (<10μM), metabolites quantified by stable isotope dilution showed
183 greater inter-day reproducibility than those analyzed by external standard calibration. Thus, due
184 to potential matrix effects and lower reproducibility, we consider the concentrations assigned by
185 external standard calibration to be semi-quantitative, in contrast to the quantitative
186 measurements made by stable isotope dilution. By either isotope dilution or external calibration,
187 we measured between 118-136 metabolites in individual experiments analyzing plasma and
188 TIF; low abundance metabolites that were not robustly and reproducibly detected were excluded
189 from individual experiments. Together, this approach allowed us to obtain a combination of
190 quantitative and semi-quantitative measurements of metabolite concentrations in both plasma
191 and TIF.
192
193 ***Pancreatic tumor TIF differs from plasma***
194 To determine if the metabolic composition of TIF differs from that of plasma, we isolated
195 TIF and plasma from PDAC tumor bearing mice. Methods of blood collection that require
196 anesthesia can alter circulating metabolite levels (Overmyer et al., 2015) (Figure 2 – figure

197 supplement 1). Therefore, to ensure that plasma samples would be directly comparable to TIF,
198 plasma samples were isolated from mice via cardiac puncture upon euthanasia.

199 PDAC TIF and plasma samples were metabolically profiled using the described
200 metabolomics techniques and grouped by either hierarchical clustering (Figure 2A) or principal
201 component analysis (Figure 2B) of metabolite concentrations. By each method, the PDAC TIF
202 samples clustered separately from the plasma samples, suggesting that the metabolic
203 composition of PDAC TIF differs from that of plasma. PDAC TIF and plasma exhibit different
204 matrix effects (Figure 2 – figure supplement 2), which could contribute to the observed global
205 differences in metabolite levels between TIF and plasma. Therefore, we also conducted a
206 comparison of PDAC TIF and plasma metabolite levels using only metabolites quantified by
207 stable isotope dilution. PDAC TIF is still substantially different from plasma when analysis is
208 limited to only metabolites quantitated using isotopically labeled internal standards (Figure 2 –
209 figure supplement 3), suggesting that the global metabolite composition of TIF differs from that
210 of plasma.

211 The composition of TIF is determined by the summed consumption and excretion rates
212 of nutrients by all cells in the tumor microenvironment and the exchange rate of those
213 metabolites between the TIF and circulation or lymph; thus, TIF composition does not allow for
214 extrapolation of the rates of consumption and excretion of nutrients from tumors. However, if the
215 exchange rate of TIF and the whole-body circulation is slow or compromised, then nutrients that
216 are highly consumed by cells within a tumor may be depleted in the TIF relative to the
217 circulation, while metabolic by-products may accumulate. Therefore, we predicted that nutrients
218 that are highly consumed by tumors and cancer cells in culture may be depleted in TIF, and
219 metabolites excreted by tumors may accumulate in TIF. Consistent with the avid consumption of
220 glucose observed in tumors and cancer cell lines, glucose was depleted in TIF compared to
221 plasma (Figure 2C-D). Amino acids known to be produced by tumors such as glycine and
222 glutamate (Hosios et al., 2016; Jain et al., 2012) were enriched in TIF (Figure 2C). Interestingly,

223 the amino acid glutamine, which is consumed rapidly by cultured cells (Eagle, 1955; Hosios et
224 al., 2016; Jain et al., 2012), was present at similar concentrations in TIF and plasma (Figure
225 2C,E). We also found that alanine, an amino acid thought to support PDAC cells (Sousa et al.,
226 2016), was abundantly present in both TIF and plasma (Figure 2F). Further, metabolites
227 important for immune cell function such as arginine, tryptophan and cystine (Geiger et al., 2016;
228 Moffett and Namboodiri, 2003; Srivastava et al., 2010) were depleted in PDAC TIF compared to
229 plasma (Figure 2C, G-I). Additionally, levels of ornithine in PDAC TIF increased relative to
230 plasma, suggesting that local arginase activity (Caldwell et al., 2018) may account for PDAC
231 depletion of arginine (Figure 2J). Many metabolites were enriched in TIF (Figure 2C),
232 suggesting that the PDAC tumor microenvironment is not depleted for all nutrients. Instead,
233 PDAC TIF is composed of a complex mix of metabolites that are different from those present in
234 circulation.
235
236 ***Tumor size does not dictate PDAC TIF composition***
237 Having established that PDAC TIF composition is different from that of plasma, we next
238 sought to understand the factors that influence TIF composition. We hypothesized that five
239 factors could influence TIF composition: tumor size, anatomical location, tumor tissue of origin,
240 diet, and tumor genetics. We used mouse models of PDAC and LUAD to systematically test the
241 impact of these factors on TIF nutrient composition. First, we sought to test if the size of tumors
242 influenced the composition of TIF. Since murine PDAC tumors cause morbidity at different times
243 and tumor sizes, we were able to isolate TIF from end stage PDAC tumors of varying sizes
244 (0.31 g – 2.81 g). We tested if tumor size significantly altered TIF composition by comparing TIF
245 metabolite concentrations between large (1.71 – 1.24 g) and small (0.78 – 1.22 g) PDAC tumors
246 (Figure 2 – figure supplement 4). We found that, at least within this size range of tumors, tumor
247 size does not appear to dictate PDAC TIF metabolite levels.
248

249 ***Tumor location affects the composition of TIF***

250 We hypothesized that PDAC tumors growing in the pancreas, with its diverse set of
251 stromal cells and poor vascularization, might have different TIF composition than the same
252 tumor cells growing in other organs or anatomical locations in the body. To test this hypothesis,
253 we compared the metabolic composition of TIF from autochthonous KP-/-C PDAC tumors to
254 that of tumors derived by subcutaneously injecting PDAC cells isolated from KP-/-C tumors into
255 genetically identical C57BL/6J mice (Figure 3A). Based on measurement of 123 quantitated
256 metabolites that were detectable and quantifiable in this experiment, PDAC TIF was
257 metabolically distinct from TIF derived from isogenic subcutaneous tumors both by principal
258 component analysis (Figure 3B) and by hierarchical clustering (Figure 3C). Interestingly,
259 concentrations of tryptophan, arginine and cystine, which are depleted in autochthonous PDAC
260 TIF, were relatively higher in subcutaneous PDAC TIF (Figure 3 D-F). This suggests that
261 subcutaneous models of PDAC may not mimic the metabolic microenvironment of PDAC
262 tumors. Furthermore, while potentially confounded by comparing transplant and autochthonous
263 PDAC models, these results suggest that the metabolic composition of TIF is not only
264 determined by tumor-intrinsic factors, but potentially also by the anatomical location in which the
265 tumor is growing.

266

267 ***Dietary changes alter TIF composition***

268 Though TIF metabolite levels do not match those found in plasma, factors that influence
269 circulating nutrient levels may be reflected in TIF. One important determinant of plasma
270 metabolite levels is diet; thus, we examined whether dietary changes would alter TIF metabolite
271 levels. For this analysis, we isolated TIF from isogenic PDAC subcutaneous allografts in mice
272 fed either standard mouse chow derived from plant and animal products or a defined diet that
273 replaces whole protein with purified amino acids (Supplementary File 2). This allows us to
274 compare genetically identical tumors growing in the same anatomical location, where only diet is

275 altered. These diets contain many differences in nutrient levels, providing a test case to
276 determine whether significant dietary alterations affect TIF metabolite levels. Based on
277 measurement of 123 metabolites that were detectable and quantifiable in this experiment, TIF
278 from mice fed standard chow differed from TIF from mice fed a defined diet based on principal
279 component analysis (Figure 4B) and hierarchical clustering (Figure 4C).

280 We next wanted to determine if the changes in TIF composition between diets were
281 primarily due to altered nutrient availability to TIF from circulation, or if other physiological
282 effects of altered diet were affecting TIF. If dietary perturbations primarily affect TIF by simply
283 altering plasma nutrient levels, then the concentration of a metabolite in TIF should correlate
284 with its concentration in plasma to the same degree in both dietary conditions. Thus, if a dietary
285 change increases the plasma level of a metabolite, then the TIF concentration of that metabolite
286 should also increase. Indeed, there is a strong correlation (Pearson r = 0.8927) between TIF to
287 plasma ratio of metabolite concentrations between mice on different diets (Figure 4D).
288 Furthermore, linear regression of TIF to plasma ratios in mice fed different diets nearly yields an
289 identity function (slope = 0.9511, R^2 = 0.7969) (Figure 4D). Thus, while individual TIF metabolite
290 levels are scaled by some factor relative to plasma levels, dietary perturbation does not broadly
291 affect this scaling factor. Thus, in addition to local microenvironmental factors, systemic
292 metabolic changes can affect the composition of TIF by altering circulating nutrient levels.
293

294 ***Tumor tissue of origin affects TIF makeup***

295 Tumor location and circulating metabolite levels are cell-extrinsic factors that influence
296 the TIF composition. However, there exist many cell-intrinsic factors that alter cancer cell
297 metabolism. For instance, the metabolic properties of cancer cells depend upon the tissue from
298 which they originated (Hu et al., 2013; Mayers et al., 2016; Yuneva et al., 2012). To examine
299 whether tissue of origin influences the metabolic makeup of the tumor microenvironment, cancer
300 cells derived from lung (Jackson et al., 2005; Jackson et al., 2001) and PDAC (Bardeesy et al.,

301 2006) tumors both driven by activation of *Kras* and loss of *Trp53* were injected subcutaneously
302 into C57BL/6J mice, such that tumors were established in the same location and with the same
303 genetics, but different tissues of origin (Figure 5A). Based on measurement of 104 metabolites
304 that were detectable and quantifiable in this experiment, TIF from subcutaneous tumors derived
305 from LUAD clustered separately from PDAC subcutaneous allograft TIF by principal component
306 analysis (Figure 5B) and hierarchical clustering (Figure 5C). Similar results were obtained when
307 the analysis was limited to only metabolites quantitated by stable isotope dilution (Figure 5 –
308 figure supplement 1). LUAD and PDAC tumors are known to have different branched-chain
309 amino acid metabolism (Mayers et al., 2016), and levels of branched-chain amino acids and
310 their catabolites were different between LUAD and PDAC tumors (Figure 5D). Additionally, a
311 number of metabolites involved in thiol metabolism are altered between LUAD and PDAC
312 tumors (Figure 5D) (Gall et al., 2010; Irino et al., 2016), suggesting potential differences in sulfur
313 metabolism between these tumors. Collectively, these data suggest that tissue of origin is a
314 determinant of the metabolic composition of TIF.
315
316 ***Genetic loss of the tumor suppressor Keap1 does not have a large effect on TIF***
317 ***composition***
318 Genetic alterations can profoundly alter cancer metabolism (Nagarajan et al., 2016). As
319 a test case for whether tumor genetics can influence the metabolism of TIF, we focused on the
320 tumor suppressor *Keap1*. *Keap1* loss is a common occurrence in lung cancer that alters
321 expression of oxidative stress response genes and nutrient transporters, which causes cells to
322 secrete high levels of glutamate and renders tumors highly dependent on glutamine catabolism
323 for growth (Romero et al., 2017; Sayin et al., 2017). Thus, *Keap1* null tumors may possess
324 remodeled metabolism that would be reflected in TIF composition. To test this possibility, we
325 injected previously described LUAD cell lines with wild-type *Keap1* (sgControl) or *Keap1* loss
326 (sg*Keap1*) (Romero et al., 2017) subcutaneously into the flanks of C57BL/6J mice (Figure 6A),

327 and TIF was isolated from these tumors. Based on measurement of 131 metabolites that were
328 detectable and quantifiable in this experiment, TIF samples did not cluster separately based on
329 *Keap1* status by principal component analysis (Figure 6B) or hierarchical clustering (Figure 6C).
330 Surprisingly, anticipated changes in TIF composition based on alterations to cancer cell
331 metabolism by *Keap1* loss, such as decreased glutamine, glucose and cystine, and increased
332 glutamate and lactate (Romero et al., 2017) were not observed between TIF samples of *Keap1*
333 wild-type and *Keap1* null tumors (Figure 6D-H). Together, these results suggest that genetic
334 *Keap1* status is not a major determinant of metabolic TIF content in subcutaneous lung cancer
335 allografts, and that not all cancer cell-intrinsic perturbations of metabolism cause detectable
336 changes to the tumor nutrient milieu.
337

338 **Discussion**

339 ***Pancreatic and lung tumor cells are exposed to nutrient levels that differ from those***
340 ***found in plasma***

341 Intravital imaging of tumors in patients (Fisher et al., 2016) and murine cancer models
342 (Fukumura et al., 2010) has revealed that solid tumors generally have abnormal and
343 dysfunctional vasculature and lymphatic vessels. For example, only ~30% of PDAC blood
344 vessels appear functional (Olive et al., 2009). This is thought to limit nutrient delivery from the
345 circulation to tumors both by reducing blood flow and by inhibiting transcapillary filtration due to
346 increased interstitial pressure (Stylianopoulos et al., 2018). PDAC tumors in particular have
347 striking defects in vasculature with numerous collapsed vessels triggered by increased
348 interstitial pressure (DuFort et al., 2016; Provenzano et al., 2012) or solid stress (Chauhan et
349 al., 2014). In contrast to normal tissues, which, while not in perfect metabolic equilibrium with
350 the circulation (Cengiz and Tamborlane, 2009), tend to have nutrient levels close to what is in
351 the circulation (Lonnroth et al., 1987), it is unlikely that the interstitial environment of tumors is in
352 rapid exchange with the circulation. Coupled with the high metabolic rate of cancer cells, this

353 has led to speculation that tumors will be both nutrient deprived and accumulate metabolic
354 wastes. We find that TIF metabolite levels in the murine cancer models assessed are different
355 from the nutrient levels in plasma. Contrary to many assumptions, not all nutrients are depleted
356 in TIF, with levels of some being higher than what is found in circulation. Thus, our
357 measurements of plasma and TIF nutrient composition are consistent with a model where
358 tumors with abnormal vasculature exist largely as a separate compartment from the bulk
359 circulation, and can have different steady state metabolic microenvironments. This underscores
360 the importance of understanding TIF composition for studies of tumor metabolism.
361 While we have considered the tumor as a single compartment and analyzed bulk TIF
362 from the entire tumor, it is possible that the tumor actually contains a population of sub-
363 compartments with different perfusion rates (Hensley et al., 2016) and heterogeneous TIF
364 compositions (Wagnerand and Wiig, 2015). Measurements of intratumor metabolites in
365 subsections of tumors suggests that some tumor regions experience different nutrient levels
366 than others (Pan et al., 2016). Thus, while the overall tumor metabolic microenvironment differs
367 from the circulation, an important future challenge will be to understand how compartmentalized
368 nutrient delivery contributes to metabolic heterogeneity observed in solid tumors (Hensley et al.,
369 2016).
370 Though TIF appears to constitute a separate compartment from plasma, tumor nutrients
371 are ultimately delivered from the circulation. Thus, perturbations to systemic nutrient levels by
372 altering diet affect TIF composition. This relationship between plasma and TIF nutrient levels
373 across different diets suggests that TIF levels of metabolites are derived from plasma metabolite
374 concentrations, and changes in plasma metabolite levels lead to scaled changes in TIF
375 metabolite levels. This argues that a major mechanism by which diet influences tumor nutrient
376 availability is by altering nutrients available in the circulation.
377
378 ***Tumor properties that influence the metabolic microenvironment***

379 Beyond dietary factors, we considered four variables that could influence tumor nutrient
380 availability: tumor size, tissue of origin, tumor anatomical location and tumor genetic make-up.
381 Though we observed that tumor size did not strongly affect the composition of TIF in PDAC
382 tumors, we collected TIF from a relatively small range of sizes of end stage PDAC tumors.
383 Future work to examine the TIF composition of tumors at various sizes and stages of
384 development may reveal effects of tumor size on TIF nutrient levels.
385 The finding that PDAC and LUAD tumors have different TIF composition suggests that
386 tissue of origin is a factor that can influence the metabolic microenvironment; however, the
387 mechanism(s) driving this difference remain unclear. Whether cancer cell-intrinsic metabolic
388 differences endowed by the epigenetic memory of the tissue of origin (Hu et al., 2013; Mayers et
389 al., 2016) or other cell-extrinsic differences between PDAC and LUAD, such as differences in
390 non-cancer cells present in the tumor, drive the difference in TIF composition is another
391 important question for future study.
392 Tumors in different anatomical locations will also contain different stromal cells and
393 different vascularization which could alter the metabolic microenvironment. Comparison of
394 autochthonous and subcutaneous PDAC tumors driven by the same oncogenic driver mutations
395 revealed significant differences in TIF nutrient levels. This suggests that subcutaneous models
396 of PDAC may not fully recapitulate the metabolic microenvironment of this disease, and is in line
397 with observations that subcutaneous models of PDAC fail to recapitulate many aspects of
398 PDAC tumors including marked stromal infiltration and extracellular matrix deposition (Hwang et
399 al., 2016). These observations, along with recent findings that subcutaneous PDAC models do
400 not recapitulate whole body metabolic perturbations observed in autochthonous PDAC models
401 and patients (Danai et al., 2018), suggest subcutaneous models do not recapitulate all
402 metabolic aspects of the disease.
403 As we compared transplant to autochthonous PDAC models, we cannot distinguish
404 between differences in TIF composition driven by anatomical location versus differences caused

405 by unique characteristics of transplant and genetically engineered PDAC models. Nevertheless,
406 it is intriguing that autochthonous PDAC tumors have lower levels of arginine, tryptophan and
407 cystine compared to subcutaneous tumors. Stromal myeloid derived cells have been implicated
408 in depleting each of these nutrients from the tumor microenvironment (Kumar et al., 2016), and
409 murine PDAC tumors are known to contain a large number of myeloid lineage cells (Bayne et
410 al., 2012; Goedegebuure et al., 2011; Stromnes et al., 2014; Zhao et al., 2009). Additionally,
411 subcutaneous PDAC tumors are known to have fewer stromal cells (Hwang et al., 2016; Sousa
412 et al., 2016). Thus, it is tempting to speculate that differences in TIF composition between
413 autochthonous and subcutaneous PDAC tumors, including differences in arginine, tryptophan
414 and cystine levels, could be driven by differences in stromal cell populations between
415 anatomical sites. Understanding how anatomical location alters the metabolic microenvironment
416 is critical to determine how local metabolic constraints shape the metabolism of tumors growing
417 in different locations, such as primary and metastatic tumors (Schild et al., 2018).
418 Lastly, we hypothesized that tumor genetics would also alter TIF composition, and
419 studied the effect of *Keap1* loss because *Keap1* null cancer cells have dramatic alterations in
420 cell-intrinsic metabolism (Best et al., 2018; DeNicola et al., 2015; DeNicola et al., 2011;
421 Mitsuishi et al., 2012; Romero et al., 2017; Sayin et al., 2017). Surprisingly, we found no
422 substantial differences in TIF composition between tumors formed from otherwise isogenic
423 LUAD cell lines that differed only in *Keap1* loss. These data argue that factors beyond cancer
424 cell-intrinsic metabolism can be dominant in setting nutrient levels in the microenvironment,
425 although future studies are required to determine how other oncogenic alterations alter TIF
426 composition.
427
428 ***Implications of TIF nutrient levels for cellular metabolism and function in the tumor***
429 It is tempting to interpret depletion or accumulation of metabolites as simply being due to
430 rapid cancer cell consumption or release of metabolites without appropriate replenishment or

431 removal from the circulation, allowing cancer cell-intrinsic changes in metabolism to be read out
432 as differences in TIF nutrient levels. However, wild type and *Keap1* null cancer cells have
433 significant changes in metabolism (Best et al., 2018; DeNicola et al., 2015; DeNicola et al.,
434 2011; Mitsuishi et al., 2012; Romero et al., 2017; Sayin et al., 2017), yet tumors derived from
435 cells of these genotypes do not show significant alterations in levels of nutrients whose
436 metabolism is known to be altered by *Keap1* loss. Thus, differences in metabolite
437 concentrations between TIF and plasma cannot be used to extrapolate consumption and
438 release of metabolites by tumors. Instead, future experiments measuring differences in arterial
439 and venous metabolite levels could shed light into quantitative tumor nutrient consumption and
440 release (Gullino et al., 1967; Kallinowski et al., 1988; Sauer et al., 1982).

441 Nutrient levels in the tumor microenvironment can have profound impacts on the
442 metabolism, growth and drug sensitivity of tumor resident cancer cells (Muir et al., 2018). Our
443 study provides insight into tumor nutrient levels *in vivo* and suggests specific implications for
444 tumor resident cell metabolism. First, we find PDAC tumor interstitial fluid is depleted of some
445 nutrients relative to plasma. Interestingly, these depleted nutrients are not necessarily
446 metabolites predicted to be depleted by cell culture studies. For example, PDAC cells consume
447 large amounts of glucose and glutamine in culture (Son et al., 2013; Ying et al., 2012), and it
448 has been assumed that these nutrients are depleted in the microenvironment (Commisso et al.,
449 2013; Kamphorst et al., 2015; Lyssiotis and Kimmelman, 2017; Sherman et al., 2017; Sousa et
450 al., 2016). Alanine and branched chain amino acids are also proposed to be limiting for
451 proliferation of PDAC cells in tumors, requiring cancer cells to acquire those nutrients from
452 alternative sources such as stromal cells or extracellular protein (Grankvist et al., 2018; Palm et
453 al., 2015; Sousa et al., 2016). We find that neither glutamine, alanine nor branched-chain amino
454 acids are substantially depleted in PDAC tumors regardless of anatomical site. Further, while
455 glucose is depleted in PDAC TIF relative to circulatory levels, it is still present at millimolar
456 concentration, and glucose deprivation in TIF is not a universal feature of tumors (Siska et al.,

457 2017). Thus, nutrients inferred from cell culture studies to be depleted and limiting in the tumor
458 microenvironment may not be always be key microenvironmental drivers altering PDAC
459 metabolism.

460 We find that the nutrient most strongly depleted from PDAC TIF is arginine. Arginine
461 supports many aspects of cell physiology (Morris, 2007), raising the question of how PDAC cells
462 adapt to survive and proliferate when levels of this amino acid are so low. Many cell types can
463 synthesize arginine using urea cycle enzymes (Wu et al., 2009), but these metabolic enzymes
464 are silenced by many tumors to enhance nucleotide production (Rabinovich et al., 2015).
465 However, PDAC tumors do not exhibit urea cycle enzyme silencing (Lee et al., 2018; Uhlen et
466 al., 2015) and are reported to have a functional urea cycle (Zaytouni et al., 2017). Perhaps,
467 PDAC cells retain this metabolic pathway to adapt to a tumor microenvironment with limited
468 arginine availability. Additionally, PDAC cells utilize macropinocytosis of environmental protein
469 (Commisso et al., 2013; Kamphorst et al., 2015), and this route of nutrient acquisition may allow
470 PDAC cells to acquire sufficient arginine to support survival and growth.

471 TIF composition can alter the function of non-cancer cells, such as immune cells, in the
472 tumor microenvironment (Buck et al., 2017). For example, in many tumor types, T lymphocytes
473 can infiltrate and inhibit the progression of tumors, especially when this process is primed with
474 checkpoint blockade treatment (Ribas and Wolchok, 2018). In contrast, PDAC tumors are highly
475 immunosuppressive (Martinez-Bosch et al., 2018) and immunotherapy shows limited efficacy in
476 this disease (Hilmi et al., 2018). Nutrient deprivation in PDAC TIF could contribute to PDAC
477 immunosuppression. Both arginine and tryptophan, which are depleted in the autochthonous
478 PDAC environment, are required for T cell function (Geiger et al., 2016; Moffett and Namboodiri,
479 2003). Intriguingly, depletion of myeloid cells capable of degrading arginine and tryptophan from
480 PDAC tumors resulted in increased T cell infiltration, proliferation, and activation in PDAC
481 tumors (Bayne et al., 2012; Stromnes et al., 2014; Zhang et al., 2017). Future studies

482 determining how T cell metabolism and function is impacted by tumor nutrient levels could yield
483 insight into how tumors suppress immune rejection (Ecker and Riley, 2018).
484 Cellular metabolism can respond and adapt to environmental nutrient levels. Indeed,
485 growing cancer cells in media with different nutrient compositions alters their metabolic
486 requirements and response to drugs (Cantor et al., 2017; Muir et al., 2017; Palm et al., 2015;
487 Schug et al., 2015). That metabolism is responsive to environment may underpin the limited
488 ability of *ex vivo* culture models using non-physiological nutrient levels to identify tumor-
489 essential metabolic genes (Horvath et al., 2016; Muir and Vander Heiden, 2018; Ryan et al.,
490 2018). However, given the dearth of information on physiological nutrient levels in solid tumors,
491 it has not been possible to determine the metabolic phenotypes and liabilities of cancer cells in
492 tumor nutrient conditions. By characterizing the polar small molecule nutrients in PDAC and
493 LUAD tumors, media that better approximates the nutrients available to cancer cells in tumors
494 can be formulated. Examining non-polar and lipid metabolites in the microenvironment will
495 further improve these efforts and lead to cancer models that may better allow us to identify
496 metabolic liabilities of cancer cells that ultimately translate into more effective therapies.
497
498 **Figure Legends**
499 **Figure 1** Stable Isotope dilution can be utilized to analyze the composition of TIF. (A) Schematic
500 of TIF isolation. (B) LDH activity assay measuring the amount of LDH present in whole tumors,
501 plasma, and TIF from PDAC tumor bearing mice. LDH activity was calculated for the entire
502 volume of TIF isolated from one tumor and plotted as a ratio to the amount of LDH present in
503 the whole tumor lysate. For each TIF sample, an equal volume of plasma was analyzed and
504 compared to the tumor lysate. n = 3 tumors, plasma, and TIF samples each. (C) LC/MS
505 measurement of equal concentrations of 70 ^{13}C chemical standards suspended in either water
506 or mouse plasma. Data are plotted as the $\log_2$ fold change between the peak area of the

507 metabolite in water versus in plasma. n = 19 plasma samples and n = 6 water samples. (D)
508 Schematic summarizing the TIF quantification method.
509
510 **Figure 1 – figure supplement 1** TIF metabolite quantification is reproducible, particularly when
511 using stable isotope dilution. Scatter plots of average LC/MS measurements of metabolite
512 concentrations across two technical replicates of 6 PDAC TIF samples run on different days
513 using either stable isotope dilution (*left*) or calibration to external standard curves (*right*). Each
514 PDAC sample was quantified twice, on different days and using different batches of ^{13}C yeast
515 extract.
516
517 **Figure 1 – source data 1** ^{13}C metabolite peak areas of metabolites suspended in plasma and
518 water for matrix effect analysis in Figure 1C.
519
520 **Figure 1 – source data 2** Metabolite concentrations in 6 PDAC TIF samples analyzed in two
521 inter-day technical replicates in Figure 1 – figure supplement 1.
522
523 **Figure 2** TIF metabolite levels are different than those in plasma. (A) Hierarchical clustering of
524 PDAC TIF and mouse plasma samples based on LC/MS measurements of 136 metabolite
525 concentrations. (B) Principal component analysis of PDAC TIF samples and mouse plasma
526 samples based on LC/MS measurements of 136 metabolite concentrations. (C) Volcano plot
527 depicting the $\log_2$ fold change in metabolite concentration between PDAC TIF and plasma. A
528 fold change of 1.5 and a raw p-value of 0.01 assuming unequal variance were used to select
529 significantly altered metabolites indicated in pink. LC/MS measurements of glucose (D),
530 glutamine (E), arginine (F), tryptophan (G), alanine (H), cystine (I), and ornithine (H) in PDAC
531 TIF and plasma samples. For all panels, n=7 for PDAC TIF and n = 18 for plasma samples.
532

533 **Figure 2 – figure supplement 1** Method of blood collection affects plasma metabolite levels.
534 Principal component analysis of mouse plasma samples based on LC/MS measurements of 117
535 metabolite concentrations from C57BL/6J mice bearing PDAC tumors. Blood was collected
536 using either retro-orbital bleeding from anesthetized mice or cardiac puncture immediately
537 following cervical dislocation of mice. n = 6 for retro-orbital blood collection, n = 7 for cardiac
538 puncture blood collection.
539
540 **Figure 2 – figure supplement 2** Plasma and TIF exhibit different matrix effects. LC/MS
541 measurement of equal concentrations of 70 ^{13}C chemical standards suspended in either mouse
542 plasma or mouse PDAC TIF. Data are plotted as the $\log_2$ fold change between the peak area of
543 the ^{13}C metabolite in water versus in plasma. n = 19 plasma samples, n = 22 TIF samples.
544
545 **Figure 2 – figure supplement 3** PDAC TIF differs from plasma when comparing only those
546 metabolites quantified using internal isotope-labeled standards. Hierarchical clustering (A) and
547 principal component analysis (B) of PDAC TIF and mouse plasma samples based on LC/MS
548 measurements of 62 metabolite concentrations using internal standards. For all panels, n=7 for
549 PDAC TIF and n = 18 for plasma samples.
550
551 **Figure 2 – figure supplement 4** PDAC TIF metabolite levels are not significantly different
552 between large and small tumors. Principal component analysis of TIF samples from large (1.71
553 – 1.24 g) and small (1.22 – 0.78 g) PDAC tumors based on LC/MS measurements of 136
554 metabolite concentrations. n=4 for large PDAC tumors and n = 3 for small PDAC tumors.
555
556 **Figure 2 – source data 1** Concentrations of 136 metabolites determined by both external
557 standard calibration and stable isotope dilution in all PDAC TIF and plasma samples in Figure 2.
558

559 **Figure 2 – source data 2** Concentrations of 117 metabolites determined by both external
560 standard calibration and stable isotope dilution for all plasma samples isolated from C57BL/6J
561 mice either by retro-orbital or cardiac puncture collection in Figure 2 – figure supplement 1.
562
563 **Figure 2 – source data 3** ^{13}C metabolite peak areas of metabolites suspended in plasma and
564 TIF for matrix effect analysis in Figure 2 – figure supplement 2.
565
566 **Figure 2 – source data 4** Concentrations of 62 metabolites determined only by stable isotope
567 dilution in all PDAC TIF and plasma samples in Figure 2 – figure supplement 3.
568
569 **Figure 3** Tumor location dictates metabolic TIF composition. (A) Diagram of experimental
570 models used to test the effect of tumor location on TIF metabolite levels. Principal component
571 analysis (B) and hierarchical clustering (C) of PDAC TIF and PDAC subcutaneous allograft TIF
572 samples based on LC/MS measurements of 123 metabolite concentrations. LC/MS
573 measurements of tryptophan (D), arginine (E), and cystine (F) in PDAC TIF and PDAC
574 subcutaneous allograft TIF. For all panels, n = 7 for PDAC TIF samples and n = 5 for PDAC
575 subcutaneous allografts.
576
577 **Figure 3 – source data 1** Concentrations of 123 metabolites determined by both external
578 standard calibration and stable isotope dilution in all autochthonous and subcutaneous PDAC
579 TIF samples in Figure 3.
580
581 **Figure 4** Dietary changes alter TIF composition. (A) Schematic of experimental models used to
582 test the effect of diet on TIF metabolite levels. Principal component analysis (B) and hierarchical
583 clustering (C) of subcutaneous PDAC allograft TIF samples from mice fed standard mouse
584 chow versus mice fed a defined diet based on LC/MS measurements of 123 metabolite

585 concentrations. (D) Ratios of LC/MS measurements of 123 metabolites in TIF versus matched
586 plasma from the same mouse fed standard mouse chow plotted versus the same ratios in mice
587 fed a defined diet. For all panels, n = 5 for TIF from mice fed standard mouse chow and n = 3
588 for TIF from mice fed a defined diet.
589
590 **Figure 4 – source data 1** Concentrations of 123 metabolites determined by both external
591 standard calibration and stable isotope dilution in all plasma and subcutaneous PDAC TIF
592 samples in Figure 4.
593
594 **Figure 5** Tumor tissue of origin influences TIF composition independent of tumor location. (A)
595 Diagram of experimental models used to test the effect of tumor tissue of origin on TIF
596 metabolite levels. Principal component analysis (B) and hierarchical clustering (C) of PDAC
597 subcutaneous allograft TIF and LUAD subcutaneous allograft TIF samples based on LC/MS
598 measurements of 104 metabolite concentrations. (D) Volcano plot depicting the $\log_2$ fold change
599 in metabolite concentration between PDAC and LUAD TIF for metabolites measured using
600 stable isotope dilution. A fold change of 1.5 and raw p-value of 0.01 assuming unequal variance
601 were used to select significantly altered metabolites indicated in pink. For all panels, n = 5 for
602 PDAC subcutaneous allograft TIF samples and n = 10 for LUAD subcutaneous allograft TIF
603 samples.
604
605 **Figure 5 – figure supplement 1** Tumor tissue of origin influences TIF when measured using
606 internal standards only. (A) Diagram of experimental models used to test the effect of tumor
607 tissue of origin on TIF metabolite levels. Principal component analysis (B) and hierarchical
608 clustering (C) of PDAC subcutaneous allograft TIF and LUAD subcutaneous allograft TIF
609 samples based on LC/MS measurements of 67 metabolites quantified using isotope-labeled

610 internal standards. For all panels, n = 5 for PDAC subcutaneous allograft TIF samples and n =
611 10 for LUAD subcutaneous allograft TIF samples.
612
613 **Figure 5 – source data 1** Concentrations of 104 metabolites determined by both external
614 standard calibration and stable isotope dilution in all subcutaneous PDAC and LUAD TIF
615 samples in Figure 5.
616
617 **Figure 5 – source data 2** Concentrations of 66 metabolites determined by only stable isotope
618 dilution in all subcutaneous PDAC and LUAD TIF samples in Figure 5 – figure supplement 1.
619
620 **Figure 6** Genetic *Keap1* status is not a major determinant of TIF composition in subcutaneous
621 LUAD allograft tumors. (A) Schematic of experimental models used to test the effect of genetic
622 loss of *Keap1* on TIF metabolite levels. Principal component analysis (B) and hierarchical
623 clustering (C) of *Keap1* wild-type (sgControl) and *Keap1* null (sgKeap1) subcutaneous LUAD
624 allograft TIF samples based on LC/MS measurements of 131 metabolite concentrations. LC/MS
625 measurements of glucose (D), lactate (E), glutamine (F), glutamate (G), and cystine (H) in
626 *Keap1* wild-type (sgControl) and *Keap1* null (sgKeap1) subcutaneous lung allograft TIF
627 samples. For all panels, n = 10 for sgControl subcutaneous lung allograft TIF samples and n = 8
628 for sgKeap1 subcutaneous LUAD allograft TIF samples.
629
630 **Figure 6 – source data 1** Concentrations of 131 metabolites determined by both external
631 standard calibration and stable isotope dilution in all sgControl and sg*Keap1* LUAD TIF samples
632 in Figure 6.
633
634 **Supplementary File 1** Information on metabolites analyzed in this study including metabolite
635 name, organization of metabolite pools, concentration of each metabolite in each metabolite

636 pool, polarity in which the metabolite was best detected, *m/z*, limit of detection, and method of
637 quantification.
638
639 **Supplementary File 2** Composition of animal diets used in this study.
640
641 **Materials and Methods**
642 ***Animal Studies***
643 All experiments performed in this study were approved by the MIT Committee on Animal
644 Care (IACUC). All mice in this study were fully backcrossed to the C57BL/6J background.
645 Animals were housed on a 12-hour light and 12-hour dark cycle, with ad libitum access to food
646 and water.
647 For studies using *Kras*^{G12D} *Trp53*$^{fl/fl}$ *Pdx-1-cre* (KP-/-C) mice (Bardeesy et al., 2006),
648 male and female animals of this genotype were allowed for form end-stage tumors, which
649 occurred approximately 8-10 weeks after birth (Danai et al., 2018). Animals were then
650 euthanized and tumors harvested for TIF isolation as described below. Tumors weighed
651 between 0.31 g – 2.81 g upon harvesting.
652 For subcutaneous xenograft studies, 12 week old C57BL/6J animals purchased from
653 Jackson Laboratories (IMSR Cat# JAX:000664, RRID:IMSR_JAX:000664) were injected with
654 100,000 murine PDAC or LUAD cancer cells (suspended in a volume of 100 µL of Matrigel
655 (Corning, 354234) brought to 10 mg/ml with RPMI-1640 (Corning, 50-020-PC) into the
656 subcutaneous space on the flank of the mice. Cell lines used for subcutaneous engraftment in
657 this study are described below. Tumors were then allowed to grow until they reached ~1cm^3 in
658 volume, which took ~4 weeks after engraftment. Upon the tumor reaching ~1cm^3, animals were
659 euthanized and tumors harvested for TIF isolation as described below.
660 For dietary studies, C57BL/6J mice were engrafted with murine PDAC cells as described
661 above. On the day of injection, the animals were separated into two cohorts. One group was fed

662 standard mouse chow and the other group was fed a defined amino acid diet (see
663 Supplementary File 2 for composition of diets). Both groups were fed each diet ad libitum
664 throughout the duration of the experiment. Upon the tumor reaching 1cm^3, animals were
665 euthanized and tumors harvested for TIF isolation as described below.
666
667 ***Cell lines and culture***
668 The murine PDAC cancer cell line (AL1376) used for making subcutaneous grafts was
669 generated as previously described (Mayers et al., 2014) from PDAC tumors from a KP-/-C
670 animal in the C57BL/6J background. The C57BL/6J LUAD cancer cell lines with and without
671 loss of *Keap1* used in tumor grafts in this study were generated previously (Romero et al., 2017)
672 from the *Kras*^{G12D} *Trp53*$^{fl/fl}$ *Adenoviral-cre* model of LUAD (Jackson et al., 2005; Jackson et al.,
673 2001). All cell lines were regularly tested for mycoplasma contamination using the Mycoprobe
674 mycoplasma detection kit (R&D Systems). All cells were cultured in a Heracell (Thermofisher)
675 humidified incubators at 37 °C and 5% CO_2. Cell lines were routinely maintained in RPMI-1640
676 (Corning, 50-020-PC) supplemented with 10% heat inactivated fetal bovine serum (Seradigm,
677 Lot 120B14).
678
679 ***Isolation of tumor interstitial fluid (TIF)***
680 TIF was isolated from tumors using a previously described centrifugal method (Eil et al.,
681 2016; Haslene-Hox et al., 2011; Ho et al., 2015; Wiig et al., 2003). Briefly, tumor bearing
682 animals were euthanized by cervical dislocation and tumors were rapidly dissected from the
683 animals. Dissections took <1 min. to complete. Blood was collected from the same animal via
684 cardiac puncture, and was immediately placed in EDTA-tubes (Sarstedt, North Rhine-
685 Westphalia, Germany) and centrifuged at 845 x g for 10 minutes at 4°C to separate plasma.
686 Plasma was frozen in liquid nitrogen and stored at -80°C until further analysis. Tumors were
687 then weighed and briefly rinsed in room temperature saline (150mM NaCl) and blotted on filter

688 paper (VWR, Radnor, PA, 28298-020). The entire process of preparing the tumor prior to
689 isolation of TIF took ~2 min. The tumors were then put onto 20μm nylon filters (Spectrum Labs,
690 Waltham, MA, 148134) affixed atop 50mL conical tubes, and centrifuged for 10 min. at 4°C at
691 106 x g. TIF was then collected from the conical tube, frozen in liquid nitrogen and stored at -
692 80°C until further analysis.
693
694 ***Quantification of lactate dehydrogenase activity in TIF, plasma and tumors***
695 To quantitate the amount of LDH activity present in TIF, plasma, and tumors, we utilized
696 the inherent absorbance of NADH at 340 nm to monitor the generation of lactate from pyruvate
697 and NADH. To an assay buffer composed of 50 mM Tris base (Sigma Aldrich, 93362), 100 mM
698 dithiothreitol (Sigma Aldrich, 646563), 180 μM NADH (Sigma Aldrich, N8129), and 500 μM
699 pyruvate (Sigma Aldrich, P5280), we added 20 μL of sample, then monitored the disappearance
700 over time of absorbance of light at 340 nM due to the consumption of NADH. A standard curve
701 of LDH (Sigma-Aldrich, 10127230001, E.C. 1.1.1.27) was generated with points of 0, 0.005838,
702 0.007783, 0.011675, 0.02335, and 0.0467 units of LDH activity by diluting LDH in Tris buffered
703 saline composed of 50 mM Tris HCl (VWR, 4103) and 150 mM NaCl (Sigma Aldrich, 746398)
704 pH adjusted to 7.5. Whole tumor samples were prepared by homogenization using a mortar and
705 pestle submerged in liquid nitrogen, and the resulting powder was resuspended at 10 mg/mL in
706 Tris buffered saline. Plasma samples were added undiluted, and TIF samples were diluted 1:10
707 in Tris buffered saline. Based on the slope of the LDH standard curve, the amount of LDH
708 activity in each sample was calculated and corrected for dilution.
709
710 ***Quantification of metabolite levels in TIF and plasma***
711 In order to quantitate metabolites in TIF and plasma samples, we first constructed a
712 library of 149 chemical standards of plasma polar metabolites (see Supplementary File 1 for
713 suppliers for each chemical standard). These compounds were selected to encompass a

714 number of metabolic processes and have previously been included in efforts to profile plasma
715 polar metabolites by LC/MS (Cantor et al., 2017; Evans et al., 2009; Lawton et al., 2008;
716 Mazzone et al., 2016). We pooled these metabolites into 7 separate chemical standard pools
717 (Supplementary File 1). To do this, each metabolite in a given pool was weighed and then
718 mixed (6 cycles of 1 min. mixing at 25 Hz followed by 3 min. resting) using a Mixer Mill MM301
719 (Retsch, Düsseldorf, Germany), and mixed metabolite powder stocks were stored at -20°C prior
720 to resuspension and analysis. Stock solutions of the mixed standards pools containing ~5mM,
721 ~1mM, ~300μM, ~100μM, ~30μM, ~10μM, ~3μM and ~1μM of each metabolite were made in
722 HPLC grade water and were stored at -80°C (see Supplementary File 1 for the concentration of
723 each metabolite in the external standard pools). We refer to these stock solutions as "external
724 standard pools" throughout. External standard pools were used to confirm the retention time and
725 *m/z* for each analyte and provide standards to quantitate concentrations of stable isotope
726 labeled internal standards used in downstream analysis, as well as to quantitate metabolite
727 concentrations in TIF and plasma samples directly where internal standards were not available
728 (see below for details).
729 To extract polar metabolites from plasma, TIF or the external standard pools, 5μL of TIF,
730 plasma or external sample pools was mixed with 45uL of acetonitrile:methanol:formic acid
731 (75:25:0.1) extraction buffer including the following isotopically labeled internal standards: ^{13}C
732 labeled yeast extract (Cambridge Isotope Laboratory, Andover, MA, ISO1), $^{13}C_3$ lactate (Sigma
733 Aldrich, Darmstadt, Germany, 485926), $^{13}C_3$ glycerol (Cambridge Isotope Laboratory, Andover,
734 MA, CLM-1510), $^{13}C_6$ $^{15}N_2$ cystine (Cambridge Isotope Laboratory, Andover, MA, CNLM-4244),
735 $^{2}H_9$ choline (Cambridge Isotope Laboratory, Andover, MA, DLM-549), $^{13}C_4$ 3-hydroxybutyrate
736 (Cambridge Isotope Laboratory, Andover, MA, CLM-3853), $^{13}C_6$ glucose (Cambridge Isotope
737 Laboratory, Andover, MA, CLM-1396), $^{13}C_2$ ^{15}N taurine (Cambridge Isotope Laboratory,
738 Andover, MA, CNLM-10253), $^{2}H_3$ creatinine (Cambridge Isotope Laboratory, Andover, MA,
739 DLM-3653), 8-^{13}C adenine (Cambridge Isotope Laboratory, Andover, MA, CLM-1654), $^{13}C_5$

740 hypoxanthine (Cambridge Isotope Laboratory, Andover, MA, CLM-8042), 8-^{13}C guanine
741 (Cambridge Isotope Laboratory, Andover, MA, CLM-1019), $^{13}C_3$ serine (Cambridge Isotope
742 Laboratory, Andover, MA, CLM-1574) and $^{13}C_2$ glycine (Cambridge Isotope Laboratory,
743 Andover, MA, CLM-1017). All solvents used in the extraction buffer were HPLC grade. Samples
744 were then vortexed for 10 min. at 4°C and insoluble material was sedimented by centrifugation
745 at 15kg for 10 min. at 4°C. 20µL of the soluble polar metabolite extract was taken for LC/MS
746 analysis.

747 LC/MS analysis was performed using a QExactive orbitrap mass spectrometer using an
748 Ion Max source and heated electrospray ionization (HESI) probe coupled to a Dionex Ultimate
749 3000 UPLC system (Thermo Fisher Scientific, Waltham, MA). External mass calibration was
750 performed every 7 days. 2µL of each sample was injected onto a ZIC-pHILIC 2.1 × 150 mm
751 analytical column equipped with a 2.1 × 20 mm guard column (both 5 µm particle size, EMD
752 Millipore). The autosampler and column oven were held at 4°C and 25°C, respectively. Buffer A
753 was 20 mM ammonium carbonate, 0.1% ammonium hydroxide; buffer B was acetonitrile. The
754 chromatographic gradient was run at a flow rate of 0.150 mL/min as follows: 0-20 min: linear
755 gradient from 80% to 20% B; 20-20.5 min: linear gradient from 20% to 80% B; 20.5-28min: hold
756 at 80% B. The mass spectrometer was operated in full scan, polarity-switching mode with the
757 spray voltage set to 3.0 kV, the heated capillary held at 275°C, and the HESI probe held at
758 350°C. The sheath gas flow rate was set to 40 units, the auxiliary gas flow was set to 15 units,
759 and the sweep gas flow was set to 1 unit. The MS data acquisition was performed in a range of
760 70-1000 m/z, with the resolution set to 70,000, the AGC target at 1e6, and the maximum
761 injection time at 20 msec.

762 Metabolite identification and quantification was performed with XCalibur 2.2 software
763 (Thermo Fisher Scientific, Waltham, MA) using a 5ppm mass accuracy and a 0.5 min. retention
764 time window. For metabolite identification, external standard pools were used for assignment of
765 metabolites to peaks at given *m/z* and retention time, and to determine the limit of detection for

766 each metabolite (see Supplementary File 1 for the *m/z*, retention time and limit of detection for
767 each metabolite analyzed). Metabolite quantification was performed by two separate methods.
768 Where internal standards were available, first, comparison of the peak areas of the stable
769 isotope labeled internal standards with the external standard pools allowed for quantification of
770 the concentration of labeled internal standards in the extraction buffer. Subsequently, we
771 compared the peak area of a given metabolite in the TIF and plasma samples with the peak
772 area of the internal standard to quantitate the concentration of that metabolite in the TIF or
773 plasma sample. 70 metabolites were quantitated using this internal standard method (see
774 Supplementary File 1 for the metabolites quantitated with internal standards). For metabolites
775 without internal standards, the peak area of each analyte was normalized to the peak area of a
776 labeled amino acid internal standard that eluted at roughly the same retention time to account
777 for differences in recovery between samples (see Supplementary File 1 for the labeled amino
778 acid paired to each metabolite analyzed without an internal standard). From the normalized
779 peak areas of metabolites in the external standard pools, we generated a standard curve
780 describing the relationship between metabolite concentration and normalized peak area. The
781 standard curves were linear with fits typically at or above r^2=0.95. Metabolites which did not
782 meet these criteria were excluded from further analysis. These equations were then used to
783 convert normalized peak areas of analytes in the TIF or plasma samples into analyte
784 concentration in the samples. 74 metabolites were quantitated using this method. The
785 relationship between metabolite concentration and normalized peak area is matrix dependent,
786 and the external standards are prepared in water, which is a different matrix than either TIF or
787 plasma. Therefore, we consider metabolite measurements using this external standard method
788 semi-quantitative.
789
790 ***Statistical analysis of TIF and plasma metabolite levels***

791 After determining the concentration of each metabolite in each plasma or TIF sample, all
792 multivariate statistical analysis on the data was performed using Metaboanalyst 4.0 (Chong et
793 al., 2018). All metabolite concentrations were not normalized prior to analysis, but the data was
794 auto-scaled (mean-centered and divided by the standard deviation of each variable) prior to
795 analysis, as this method of scaling has been shown to perform well with metabolomics data (van
796 den Berg et al., 2006). After scaling the data, we performed principal component analysis and
797 hierarchical clustering with Euclidean distance measurement and clustering by the Ward
798 algorithm. Univariate analysis was performed comparing metabolite levels between groups
799 where metabolite differences of interest were defined by a fold change greater than 1.5 and
800 significance as a FDR-adjusted P-value less than 0.1 assuming unequal group variance. All
801 other statistical analysis and graphical representation of data was performed as described in the
802 **Results** using GraphPad Prism 7 (GraphPad Software, La Jolla, CA).
803

804 **Acknowledgements**

805 We thank Aaron Hosios and all members of the Vander Heiden lab for many useful
806 discussions and experimental advice, and Allison Lau and Sharanya Sivanand for supplying
807 tumor bearing animals used in this work. We thank Sarah Price for assistance with developing
808 data analysis tools. We thank Peggy Hsu, Alicia Darnell, and Allison Lau for comments and help
809 with editing the manuscript. We thank Rodrigo Romero and Tyler Jacks for generously
810 supplying murine LUAD cell lines and providing experimental advice. We thank Susan Kaech,
811 Victor Chubakov and Thomas Roddy for helpful discussions on interstitial fluid isolation and
812 analysis. Lastly, we thank Cambridge Isotope Laboratories for the generous gift of isotopically
813 labeled yeast extract used in this work. This work was supported by grants to M.G.V.H. from the
814 NIH (R01CA168653, R01CA201276, and P30CA1405141), the Lustgarten Foundation, the MIT
815 Center for Precision Medicine, SU2C, and the Ludwig Center at MIT. A.M. and L.V.D. were
816 supported by NIH Ruth Kirschstein Fellowships, F32CA213810 and F32CA210421 respectively.

817 M.R.S. was supported by T32GM007287 and acknowledges additional support from an MIT
818 Koch Institute Graduate Fellowship. D.Y.G. received support from T32GM007753. M.G.V.H. is a
819 Howard Hughes Medical Institute Faculty Scholar.

820

821 **Competing interests**

822 M.G.V.H., A.M., L.V.D. and D.Y.G. have applied for patents for therapeutic strategies to target
823 cancer metabolism. M.G.V.H. is on the scientific advisory board of Agios Pharmaceuticals,
824 Aeglea Biotherapeutics, and Auron Therapeutics, which seek to exploit altered metabolism for
825 therapy.

826

827

828 **References**

829 Alvarez, S.W., Sviderskiy, V.O., Terzi, E.M., Papagiannakopoulos, T., Moreira, A.L., Adams, S.,
830 Sabatini, D.M., Birsoy, K., and Possemato, R. (2017). NFS1 undergoes positive
831 selection in lung tumours and protects cells from ferroptosis. Nature *551*, 639-643.
832 Anastasiou, D. (2017). Tumour microenvironment factors shaping the cancer metabolism
833 landscape. Br J Cancer *116*, 277-286.
834 Bardeesy, N., Aguirre, A.J., Chu, G.C., Cheng, K.H., Lopez, L.V., Hezel, A.F., Feng, B.,
835 Brennan, C., Weissleder, R., Mahmood, U.*, et al.* (2006). Both p16(Ink4a) and the
836 p19(Arf)-p53 pathway constrain progression of pancreatic adenocarcinoma in the
837 mouse. Proc Natl Acad Sci U S A *103*, 5947-5952.
838 Bayne, L.J., Beatty, G.L., Jhala, N., Clark, C.E., Rhim, A.D., Stanger, B.Z., and Vonderheide,
839 R.H. (2012). Tumor-derived granulocyte-macrophage colony-stimulating factor regulates
840 myeloid inflammation and T cell immunity in pancreatic cancer. Cancer Cell *21*, 822-835.
841 Best, S.A., De Souza, D.P., Kersbergen, A., Policheni, A.N., Dayalan, S., Tull, D., Rathi, V.,
842 Gray, D.H., Ritchie, M.E., McConville, M.J.*, et al.* (2018). Synergy between the
843 KEAP1/NRF2 and PI3K Pathways Drives Non-Small-Cell Lung Cancer with an Altered
844 Immune Microenvironment. Cell Metabolism *27*, 935-+.
845 Bi, J.F., Wu, S.H., Zhang, W.J., and Mischel, P.S. (2018). Targeting cancer's metabolic co-
846 dependencies: A landscape shaped by genotype and tissue context. Bba-Rev Cancer
847 *1870*, 76-87.
848 Biancur, D.E., Paulo, J.A., Malachowska, B., Del Rey, M.Q., Sousa, C.M., Wang, X., Sohn,
849 A.S.W., Chu, G.C., Gygi, S.P., Harper, J.W.*, et al.* (2017). Compensatory metabolic
850 networks in pancreatic cancers upon perturbation of glutamine metabolism. Nat
851 Commun *8*, 15965.
852 Buck, M.D., Sowell, R.T., Kaech, S.M., and Pearce, E.L. (2017). Metabolic Instruction of
853 Immunity. Cell *169*, 570-586.
854 Burgess, E.A., and Sylven, B. (1962). Glucose, lactate, and lactic dehydrogenase activity in
855 normal interstitial fluid and that of solid mouse tumors. Cancer Res *22*, 581-588.

856 Caldwell, R.W., Rodriguez, P.C., Toque, H.A., Narayanan, S.P., and Caldwell, R.B. (2018).
857 Arginase: A Multifaceted Enzyme Important in Health and Disease. Physiol Rev *98*, 641-
858 665.
859 Cantor, J.R., Abu-Remaileh, M., Kanarek, N., Freinkman, E., Gao, X., Louissaint, A., Jr., Lewis,
860 C.A., and Sabatini, D.M. (2017). Physiologic Medium Rewires Cellular Metabolism and
861 Reveals Uric Acid as an Endogenous Inhibitor of UMP Synthase. Cell *169*, 258-272
862 e217.
863 Cengiz, E., and Tamborlane, W.V. (2009). A tale of two compartments: interstitial versus blood
864 glucose monitoring. Diabetes Technol Ther *11 Suppl 1*, S11-16.
865 Chauhan, V.P., Boucher, Y., Ferrone, C.R., Roberge, S., Martin, J.D., Stylianopoulos, T.,
866 Bardeesy, N., DePinho, R.A., Padera, T.P., Munn, L.L.*, et al.* (2014). Compression of
867 Pancreatic Tumor Blood Vessels by Hyaluronan Is Caused by Solid Stress and Not
868 Interstitial Fluid Pressure. Cancer Cell *26*, 14-15.
869 Chen, W.W., Freinkman, E., Wang, T., Birsoy, K., and Sabatini, D.M. (2016). Absolute
870 Quantification of Matrix Metabolites Reveals the Dynamics of Mitochondrial Metabolism.
871 Cell *166*, 1324-1337 e1311.
872 Chong, J., Soufan, O., Li, C., Caraus, I., Li, S., Bourque, G., Wishart, D.S., and Xia, J. (2018).
873 MetaboAnalyst 4.0: towards more transparent and integrative metabolomics analysis.
874 Nucleic Acids Res *46*, W486-W494.
875 Commisso, C., Davidson, S.M., Soydaner-Azeloglu, R.G., Parker, S.J., Kamphorst, J.J.,
876 Hackett, S., Grabocka, E., Nofal, M., Drebin, J.A., Thompson, C.B.*, et al.* (2013).
877 Macropinocytosis of protein is an amino acid supply route in Ras-transformed cells.
878 Nature *497*, 633-+.
879 Corbet, C., and Feron, O. (2017). Tumour acidosis: from the passenger to the driver's seat. Nat
880 Rev Cancer *17*, 577-593.
881 Cori, C.F., and Cori, G.T. (1925). The carbohydrate metabolism of tumors. II. Changes in the
882 sugar, lactic acid, and co-combing power of blood passing through a tumor. Journal of
883 Biological Chemistry *65*, 397-405.
884 Danai, L.V., Babic, A., Rosenthal, M.H., Dennstedt, E.A., Muir, A., Lien, E.C., Mayers, J.R., Tai,
885 K., Lau, A.N., Jones-Sali, P.*, et al.* (2018). Altered exocrine function can drive adipose
886 wasting in early pancreatic cancer. Nature.
887 Davidson, S.M., Papagiannakopoulos, T., Olenchock, B.A., Heyman, J.E., Keibler, M.A.,
888 Luengo, A., Bauer, M.R., Jha, A.K., O'Brien, J.P., Pierce, K.A.*, et al.* (2016).
889 Environment Impacts the Metabolic Dependencies of Ras-Driven Non-Small Cell Lung
890 Cancer. Cell Metab *23*, 517-528.
891 DeBerardinis, R.J., and Chandel, N.S. (2016). Fundamentals of cancer metabolism. Sci Adv *2*,
892 e1600200.
893 DelNero, P., Hopkins, B.D., Cantley, L.C., and Fischbach, C. (2018). Cancer metabolism gets
894 physical. Sci Transl Med *10*.
895 DeNicola, G.M., Chen, P.H., Mullarky, E., Sudderth, J.A., Hu, Z., Wu, D., Tang, H., Xie, Y.,
896 Asara, J.M., Huffman, K.E.*, et al.* (2015). NRF2 regulates serine biosynthesis in non-
897 small cell lung cancer. Nat Genet *47*, 1475-1481.
898 DeNicola, G.M., Karreth, F.A., Humpton, T.J., Gopinathan, A., Wei, C., Frese, K., Mangal, D.,
899 Yu, K.H., Yeo, C.J., Calhoun, E.S.*, et al.* (2011). Oncogene-induced Nrf2 transcription
900 promotes ROS detoxification and tumorigenesis. Nature *475*, 106-109.
901 DuFort, C.C., DelGiorno, K.E., Carlson, M.A., Osgood, R.J., Zhao, C.M., Huang, Z.D.,
902 Thompson, C.B., Connor, R.J., Thanos, C.D., Brockenbrough, J.S.*, et al.* (2016).
903 Interstitial Pressure in Pancreatic Ductal Adenocarcinoma Is Dominated by a Gel-Fluid
904 Phase. Biophysical Journal *110*, 2106-2119.
905 Eagle, H. (1955). Nutrition needs of mammalian cells in tissue culture. Science *122*, 501-514.

906 Ecker, C., and Riley, J.L. (2018). Translating In Vitro T Cell Metabolic Findings to In Vivo Tumor
907 Models of Nutrient Competition. Cell Metabolism *28*, 190-195.
908 Eil, R., Vodnala, S.K., Clever, D., Klebanoff, C.A., Sukumar, M., Pan, J.H., Palmer, D.C., Gros,
909 A., Yamamoto, T.N., Patel, S.J.*, et al.* (2016). Ionic immune suppression within the
910 tumour microenvironment limits T cell effector function. Nature *537*, 539-+.
911 Evans, A.M., DeHaven, C.D., Barrett, T., Mitchell, M., and Milgram, E. (2009). Integrated,
912 nontargeted ultrahigh performance liquid chromatography/electrospray ionization
913 tandem mass spectrometry platform for the identification and relative quantification of
914 the small-molecule complement of biological systems. Anal Chem *81*, 6656-6667.
915 Fisher, D.T., Muhitch, J.B., Kim, M., Doyen, K.C., Bogner, P.N., Evans, S.S., and Skitzki, J.J.
916 (2016). Intraoperative intravital microscopy permits the study of human tumour vessels.
917 Nat Commun *7*, 10684.
918 Fukumura, D., Duda, D.G., Munn, L.L., and Jain, R.K. (2010). Tumor Microvasculature and
919 Microenvironment: Novel Insights Through Intravital Imaging in Pre-Clinical Models.
920 Microcirculation *17*, 206-225.
921 Gall, W.E., Beebe, K., Lawton, K.A., Adam, K.P., Mitchell, M.W., Nakhle, P.J., Ryals, J.A.,
922 Milburn, M.V., Nannipieri, M., Camastra, S.*, et al.* (2010). alpha-Hydroxybutyrate Is an
923 Early Biomarker of Insulin Resistance and Glucose Intolerance in a Nondiabetic
924 Population. Plos One *5*.
925 Geiger, R., Rieckmann, J.C., Wolf, T., Basso, C., Feng, Y., Fuhrer, T., Kogadeeva, M., Picotti,
926 P., Meissner, F., Mann, M.*, et al.* (2016). L-Arginine Modulates T Cell Metabolism and
927 Enhances Survival and Anti-tumor Activity. Cell *167*, 829-842 e813.
928 Goedegebuure, P., Mitchem, J.B., Porembka, M.R., Tan, M.C., Belt, B.A., Wang-Gillam, A.,
929 Gillanders, W.E., Hawkins, W.G., and Linehan, D.C. (2011). Myeloid-derived suppressor
930 cells: general characteristics and relevance to clinical management of pancreatic cancer.
931 Curr Cancer Drug Targets *11*, 734-751.
932 Grankvist, N., Watrous, J.D., Lagerborg, K.A., Lyutvinskiy, Y., Jain, M., and Nilsson, R. (2018).
933 Profiling the Metabolism of Human Cells by Deep (13)C Labeling. Cell Chem Biol.
934 Gui, D.Y., Sullivan, L.B., Luengo, A., Hosios, A.M., Bush, L.N., Gitego, N., Davidson, S.M.,
935 Freinkman, E., Thomas, C.J., and Vander Heiden, M.G. (2016). Environment Dictates
936 Dependence on Mitochondrial Complex I for NAD+ and Aspartate Production and
937 Determines Cancer Cell Sensitivity to Metformin. Cell Metab *24*, 716-727.
938 Gullino, P.M., Clark, S.H., and Grantham, F.H. (1964). The Interstitial Fluid of Solid Tumors.
939 Cancer Res *24*, 780-794.
940 Gullino, P.M., Grantham, F.H., and Courtney, A.H. (1967). Glucose consumption by
941 transplanted tumors in vivo. Cancer Res *27*, 1031-1040.
942 Haslene-Hox, H., Oveland, E., Berg, K.C., Kolmannskog, O., Woie, K., Salvesen, H.B., Tenstad,
943 O., and Wiig, H. (2011). A new method for isolation of interstitial fluid from human solid
944 tumors applied to proteomic analysis of ovarian carcinoma tissue. PLoS One *6*, e19217.
945 Hensley, C.T., Faubert, B., Yuan, Q., Lev-Cohain, N., Jin, E., Kim, J., Jiang, L., Ko, B., Skelton,
946 R., Loudat, L.*, et al.* (2016). Metabolic Heterogeneity in Human Lung Tumors. Cell *164*,
947 681-694.
948 Hermann, G., Schwaiger, M., Volejnik, P., and Koellensperger, G. (2018). (13)C-labelled yeast
949 as internal standard for LC-MS/MS and LC high resolution MS based amino acid
950 quantification in human plasma. J Pharm Biomed Anal *155*, 329-334.
951 Hilmi, M., Bartholin, L., and Neuzillet, C. (2018). Immune therapies in pancreatic ductal
952 adenocarcinoma: Where are we now? World J Gastroenterol *24*, 2137-2151.
953 Ho, P.C., Bihuniak, J.D., Macintyre, A.N., Staron, M., Liu, X.J., Amezquita, R., Tsui, Y.C., Cui,
954 G.L., Micevic, G., Perales, J.C.*, et al.* (2015). Phosphoenolpyruvate Is a Metabolic
955 Checkpoint of Anti-tumor T Cell Responses. Cell *162*, 1217-1228.

956 Horvath, P., Aulner, N., Bickle, M., Davies, A.M., Nery, E.D., Ebner, D., Montoya, M.C., Ostling,
957 P., Pietiainen, V., Price, L.S.*, et al.* (2016). Screening out irrelevant cell-based models of
958 disease. Nat Rev Drug Discov *15*, 751-769.
959 Hosios, A.M., Hecht, V.C., Danai, L.V., Johnson, M.O., Rathmell, J.C., Steinhauser, M.L.,
960 Manalis, S.R., and Vander Heiden, M.G. (2016). Amino Acids Rather than Glucose
961 Account for the Majority of Cell Mass in Proliferating Mammalian Cells. Dev Cell *36*, 540-
962 549.
963 Hu, J., Locasale, J.W., Bielas, J.H., O'Sullivan, J., Sheahan, K., Cantley, L.C., Vander Heiden,
964 M.G., and Vitkup, D. (2013). Heterogeneity of tumor-induced gene expression changes
965 in the human metabolic network. Nat Biotechnol *31*, 522-529.
966 Hwang, C.I., Boj, S.F., Clevers, H., and Tuveson, D.A. (2016). Preclinical models of pancreatic
967 ductal adenocarcinoma. J Pathol *238*, 197-204.
968 Irino, Y., Toh, R., Nagao, M., Mori, T., Honjo, T., Shinohara, M., Tsuda, S., Nakajima, H.,
969 Satomi-Kobayashi, S., Shinke, T.*, et al.* (2016). 2-Aminobutyric acid modulates
970 glutathione homeostasis in the myocardium. Sci Rep *6*, 36749.
971 Jackson, E.L., Olive, K.P., Tuveson, D.A., Bronson, R., Crowley, D., Brown, M., and Jacks, T.
972 (2005). The differential effects of mutant p53 alleles on advanced murine lung cancer.
973 Cancer Research *65*, 10280-10288.
974 Jackson, E.L., Willis, N., Mercer, K., Bronson, R.T., Crowley, D., Montoya, R., Jacks, T., and
975 Tuveson, D.A. (2001). Analysis of lung tumor initiation and progression using conditional
976 expression of oncogenic K-ras. Gene Dev *15*, 3243-3248.
977 Jain, M., Nilsson, R., Sharma, S., Madhusudhan, N., Kitami, T., Souza, A.L., Kafri, R.,
978 Kirschner, M.W., Clish, C.B., and Mootha, V.K. (2012). Metabolite profiling identifies a
979 key role for glycine in rapid cancer cell proliferation. Science *336*, 1040-1044.
980 Kallinowski, F., Vaupel, P., Runkel, S., Berg, G., Fortmeyer, H.P., Baessler, K.H., Wagner, K.,
981 Mueller-Klieser, W., and Walenta, S. (1988). Glucose uptake, lactate release, ketone
982 body turnover, metabolic micromilieu, and pH distributions in human breast cancer
983 xenografts in nude rats. Cancer Res *48*, 7264-7272.
984 Kamphorst, J.J., Nofal, M., Commisso, C., Hackett, S.R., Lu, W., Grabocka, E., Vander Heiden,
985 M.G., Miller, G., Drebin, J.A., Bar-Sagi, D.*, et al.* (2015). Human pancreatic cancer
986 tumors are nutrient poor and tumor cells actively scavenge extracellular protein. Cancer
987 Res *75*, 544-553.
988 Koong, A.C., Mehta, V.K., Le, Q.T., Fisher, G.A., Terris, D.J., Brown, J.M., Bastidas, A.J., and
989 Vierra, M. (2000). Pancreatic tumors show high levels of hypoxia. Int J Radiat Oncol *48*,
990 919-922.
991 Koppenol, W.H., Bounds, P.L., and Dang, C.V. (2011). Otto Warburg's contributions to current
992 concepts of cancer metabolism. Nat Rev Cancer *11*, 325-337.
993 Kumar, V., Patel, S., Tcyganov, E., and Gabrilovich, D.I. (2016). The Nature of Myeloid-Derived
994 Suppressor Cells in the Tumor Microenvironment. Trends Immunol *37*, 208-220.
995 Lawton, K.A., Berger, A., Mitchell, M., Milgram, K.E., Evans, A.M., Guo, L., Hanson, R.W.,
996 Kalhan, S.C., Ryals, J.A., and Milburn, M.V. (2008). Analysis of the adult human plasma
997 metabolome. Pharmacogenomics *9*, 383-397.
998 Lee, J.S., Adler, L., Karathia, H., Carmel, N., Rabinovich, S., Auslander, N., Keshet, R.,
999 Stettner, N., Silberman, A., Agemy, L.*, et al.* (2018). Urea Cycle Dysregulation
1000 Generates Clinically Relevant Genomic and Biochemical Signatures. Cell *174*, 1559-+.
1001 Lonnroth, P., Jansson, P.A., and Smith, U. (1987). A Microdialysis Method Allowing
1002 Characterization of Intercellular Water Space in Humans. Am J Physiol *253*, E228-E231.
1003 Lyssiotis, C.A., and Kimmelman, A.C. (2017). Metabolic Interactions in the Tumor
1004 Microenvironment. Trends Cell Biol *27*, 863-875.
1005 Martinez-Bosch, N., Vinaixa, J., and Navarro, P. (2018). Immune Evasion in Pancreatic Cancer:
1006 From Mechanisms to Therapy. Cancers *10*.

1007 Mayers, J.R., Torrence, M.E., Danai, L.V., Papagiannakopoulos, T., Davidson, S.M., Bauer,
1008 M.R., Lau, A.N., Ji, B.W., Dixit, P.D., Hosios, A.M.*, et al.* (2016). Tissue of origin dictates
1009 branched-chain amino acid metabolism in mutant Kras-driven cancers. Science *353*,
1010 1161-1165.
1011 Mayers, J.R., Wu, C., Clish, C.B., Kraft, P., Torrence, M.E., Fiske, B.P., Yuan, C., Bao, Y.,
1012 Townsend, M.K., Tworoger, S.S.*, et al.* (2014). Elevation of circulating branched-chain
1013 amino acids is an early event in human pancreatic adenocarcinoma development. Nat
1014 Med *20*, 1193-1198.
1015 Mazzone, P.J., Wang, X.F., Beukemann, M., Zhang, Q., Seeley, M., Mohney, R., Holt, T., and
1016 Pappan, K.L. (2016). Metabolite Profiles of the Serum of Patients with Non-Small Cell
1017 Carcinoma. J Thorac Oncol *11*, 72-78.
1018 Mitsuishi, Y., Taguchi, K., Kawatani, Y., Shibata, T., Nukiwa, T., Aburatani, H., Yamamoto, M.,
1019 and Motohashi, H. (2012). Nrf2 redirects glucose and glutamine into anabolic pathways
1020 in metabolic reprogramming. Cancer Cell *22*, 66-79.
1021 Moffett, J.R., and Namboodiri, M.A. (2003). Tryptophan and the immune response. Immunol
1022 Cell Biol *81*, 247-265.
1023 Morandi, A., Giannoni, E., and Chiarugi, P. (2016). Nutrient Exploitation within the Tumor-
1024 Stroma Metabolic Crosstalk. Trends Cancer *2*, 736-746.
1025 Morris, S.M. (2007). Arginine metabolism: Boundaries of our knowledge. J Nutr *137*, 1602s-
1026 1609s.
1027 Muir, A., Danai, L.V., Gui, D.Y., Waingarten, C.Y., Lewis, C.A., and Vander Heiden, M.G.
1028 (2017). Environmental cystine drives glutamine anaplerosis and sensitizes cancer cells
1029 to glutaminase inhibition. Elife *6*.
1030 Muir, A., Danai, L.V., and Vander Heiden, M.G. (2018). Microenvironmental regulation of cancer
1031 cell metabolism: implications for experimental design and translational studies. Dis
1032 Model Mech *11*.
1033 Muir, A., and Vander Heiden, M.G. (2018). The nutrient environment affects therapy. Science
1034 *360*, 962-963.
1035 Nagarajan, A., Malvi, P., and Wajapeyee, N. (2016). Oncogene-directed alterations in cancer
1036 cell metabolism. Trends Cancer *2*, 365-377.
1037 Olive, K.P., Jacobetz, M.A., Davidson, C.J., Gopinathan, A., McIntyre, D., Honess, D., Madhu,
1038 B., Goldgraben, M.A., Caldwell, M.E., Allard, D.*, et al.* (2009). Inhibition of Hedgehog
1039 signaling enhances delivery of chemotherapy in a mouse model of pancreatic cancer.
1040 Science *324*, 1457-1461.
1041 Overmyer, K.A., Thonusin, C., Qi, N.R., Burant, C.F., and Evans, C.R. (2015). Impact of
1042 anesthesia and euthanasia on metabolomics of mammalian tissues: studies in a
1043 C57BL/6J mouse model. PLoS One *10*, e0117232.
1044 Palm, W., Park, Y., Wright, K., Pavlova, N.N., Tuveson, D.A., and Thompson, C.B. (2015). The
1045 Utilization of Extracellular Proteins as Nutrients Is Suppressed by mTORC1. Cell *162*,
1046 259-270.
1047 Pan, M., Reid, M.A., Lowman, X.H., Kulkarni, R.P., Tran, T.Q., Liu, X.J., Yang, Y., Hernandez-
1048 Davies, J.E., Rosales, K.K., Li, H.Q.*, et al.* (2016). Regional glutamine deficiency in
1049 tumours promotes dedifferentiation through inhibition of histone demethylation. Nature
1050 Cell Biology *18*, 1090-1101.
1051 Persi, E., Duran-Frigola, M., Damaghi, M., Roush, W.R., Aloy, P., Cleveland, J.L., Gillies, R.J.,
1052 and Ruppin, E. (2018). Systems analysis of intracellular pH vulnerabilities for cancer
1053 therapy. Nature Communications *9*.
1054 Possemato, R., Marks, K.M., Shaul, Y.D., Pacold, M.E., Kim, D., Birsoy, K., Sethumadhavan,
1055 S., Woo, H.K., Jang, H.G., Jha, A.K.*, et al.* (2011). Functional genomics reveal that the
1056 serine synthesis pathway is essential in breast cancer. Nature *476*, 346-350.

1057 Provenzano, P.P., Cuevas, C., Chang, A.E., Goel, V.K., Von Hoff, D.D., and Hingorani, S.R.
1058 (2012). Enzymatic targeting of the stroma ablates physical barriers to treatment of
1059 pancreatic ductal adenocarcinoma. Cancer Cell *21*, 418-429.
1060 Rabinovich, S., Adler, L., Yizhak, K., Sarver, A., Silberman, A., Agron, S., Stettner, N., Sun, Q.,
1061 Brandis, A., Helbling, D.*, et al.* (2015). Diversion of aspartate in ASS1-deficient tumours
1062 fosters de novo pyrimidine synthesis. Nature *527*, 379-+.
1063 Ribas, A., and Wolchok, J.D. (2018). Cancer immunotherapy using checkpoint blockade.
1064 Science *359*, 1350-+.
1065 Romero, R., Sayin, V.I., Davidson, S.M., Bauer, M.R., Singh, S.X., LeBoeuf, S.E., Karakousi,
1066 T.R., Ellis, D.C., Bhutkar, A., Sanchez-Rivera, F.J.*, et al.* (2017). Keap1 loss promotes
1067 Kras-driven lung cancer and results in dependence on glutaminolysis. Nat Med *23*,
1068 1362-1368.
1069 Ryan, C.J., Bajrami, I., and Lord, C.J. (2018). Synthetic Lethality and Cancer - Penetrance as
1070 the Major Barrier. Trends in Cancer *4*, 671-683.
1071 Sauer, L.A., Stayman, J.W., 3rd, and Dauchy, R.T. (1982). Amino acid, glucose, and lactic acid
1072 utilization in vivo by rat tumors. Cancer Res *42*, 4090-4097.
1073 Sayin, V.I., LeBoeuf, S.E., Singh, S.X., Davidson, S.M., Biancur, D., Guzelhan, B.S., Alvarez,
1074 S.W., Wu, W.L., Karakousi, T.R., Zavitsanou, A.M.*, et al.* (2017). Activation of the NRF2
1075 antioxidant program generates an imbalance in central carbon metabolism in cancer.
1076 Elife *6*.
1077 Schild, T., Low, V., Blenis, J., and Gomes, A.P. (2018). Unique Metabolic Adaptations Dictate
1078 Distal Organ-Specific Metastatic Colonization. Cancer Cell *33*, 347-354.
1079 Schug, Z.T., Peck, B., Jones, D.T., Zhang, Q., Grosskurth, S., Alam, I.S., Goodwin, L.M.,
1080 Smethurst, E., Mason, S., Blyth, K.*, et al.* (2015). Acetyl-CoA synthetase 2 promotes
1081 acetate utilization and maintains cancer cell growth under metabolic stress. Cancer Cell
1082 *27*, 57-71.
1083 Sellers, K., Fox, M.P., Bousamra, M., 2nd, Slone, S.P., Higashi, R.M., Miller, D.M., Wang, Y.,
1084 Yan, J., Yuneva, M.O., Deshpande, R.*, et al.* (2015). Pyruvate carboxylase is critical for
1085 non-small-cell lung cancer proliferation. J Clin Invest *125*, 687-698.
1086 Sherman, M.H., Yu, R.T., Tseng, T.W., Sousa, C.M., Liu, S.H., Truitt, M.L., He, N.H., Ding, N.,
1087 Liddle, C., Atkins, A.R.*, et al.* (2017). Stromal cues regulate the pancreatic cancer
1088 epigenome and metabolome. P Natl Acad Sci USA *114*, 1129-1134.
1089 Siska, P.J., Beckermann, K.E., Mason, F.M., Andrejeva, G., Greenplate, A.R., Sendor, A.B.,
1090 Chiang, Y.J., Corona, A.L., Gemta, L.F., Vincent, B.G.*, et al.* (2017). Mitochondrial
1091 dysregulation and glycolytic insufficiency functionally impair CD8 T cells infiltrating
1092 human renal cell carcinoma. JCI Insight *2*.
1093 Son, J., Lyssiotis, C.A., Ying, H.Q., Wang, X.X., Hua, S.J., Ligorio, M., Perera, R.M., Ferrone,
1094 C.R., Mullarky, E., Shyh-Chang, N.*, et al.* (2013). Glutamine supports pancreatic cancer
1095 growth through a KRAS-regulated metabolic pathway (vol 496, pg 101, 2013). Nature
1096 *499*.
1097 Sousa, C.M., Biancur, D.E., Wang, X., Halbrook, C.J., Sherman, M.H., Zhang, L., Kremer, D.,
1098 Hwang, R.F., Witkiewicz, A.K., Ying, H.*, et al.* (2016). Pancreatic stellate cells support
1099 tumour metabolism through autophagic alanine secretion. Nature *536*, 479-483.
1100 Srivastava, M.K., Sinha, P., Clements, V.K., Rodriguez, P., and Ostrand-Rosenberg, S. (2010).
1101 Myeloid-Derived Suppressor Cells Inhibit T-Cell Activation by Depleting Cystine and
1102 Cysteine. Cancer Research *70*, 68-77.
1103 Stromnes, I.M., Brockenbrough, J.S., Izeradjene, K., Carlson, M.A., Cuevas, C., Simmons,
1104 R.M., Greenberg, P.D., and Hingorani, S.R. (2014). Targeted depletion of an MDSC
1105 subset unmasks pancreatic ductal adenocarcinoma to adaptive immunity. Gut *63*, 1769-
1106 1781.

1107 Stylianopoulos, T., Munn, L.L., and Jain, R.K. (2018). Reengineering the Physical
1108 Microenvironment of Tumors to Improve Drug Delivery and Efficacy: From Mathematical
1109 Modeling to Bench to Bedside. Trends in Cancer *4*, 292-319.
1110 Tardito, S., Oudin, A., Ahmed, S.U., Fack, F., Keunen, O., Zheng, L., Miletic, H., Sakariassen,
1111 P.O., Weinstock, A., Wagner, A.*, et al.* (2015). Glutamine synthetase activity fuels
1112 nucleotide biosynthesis and supports growth of glutamine-restricted glioblastoma. Nat
1113 Cell Biol *17*, 1556-1568.
1114 Trufelli, H., Palma, P., Famiglini, G., and Cappiello, A. (2011). An overview of matrix effects in
1115 liquid chromatography-mass spectrometry. Mass Spectrom Rev *30*, 491-509.
1116 Tung, J.C., Barnes, J.M., Desai, S.R., Sistrunk, C., Conklin, M.W., Schedin, P., Eliceiri, K.W.,
1117 Keely, P.J., Seewaldt, V.L., and Weaver, V.M. (2015). Tumor mechanics and metabolic
1118 dysfunction. Free Radic Biol Med *79*, 269-280.
1119 Uhlen, M., Fagerberg, L., Hallstrom, B.M., Lindskog, C., Oksvold, P., Mardinoglu, A., Sivertsson,
1120 A., Kampf, C., Sjostedt, E., Asplund, A.*, et al.* (2015). Tissue-based map of the human
1121 proteome. Science *347*.
1122 van den Berg, R.A., Hoefsloot, H.C.J., Westerhuis, J.A., Smilde, A.K., and van der Werf, M.J.
1123 (2006). Centering, scaling, and transformations: improving the biological information
1124 content of metabolomics data. Bmc Genomics *7*.
1125 Wagnerand, M., and Wiig, H. (2015). Tumor interstitial fluid formation, characterization, and
1126 clinical implications. Front Oncol *5*.
1127 Wiig, H., Aukland, K., and Tenstad, O. (2003). Isolation of interstitial fluid from rat mammary
1128 tumors by a centrifugation method. Am J Physiol Heart Circ Physiol *284*, H416-424.
1129 Wiig, H., and Swartz, M.A. (2012). Interstitial Fluid and Lymph Formation and Transport:
1130 Physiological Regulation and Roles in Inflammation and Cancer. Physiol Rev *92*, 1005-
1131 1060.
1132 Wolpaw, A.J., and Dang, C.V. (2018). Exploiting Metabolic Vulnerabilities of Cancer with
1133 Precision and Accuracy. Trends Cell Biol *28*, 201-212.
1134 Wu, G.Y., Bazer, F.W., Davis, T.A., Kim, S.W., Li, P., Rhoads, J.M., Satterfield, M.C., Smith,
1135 S.B., Spencer, T.E., and Yin, Y.L. (2009). Arginine metabolism and nutrition in growth,
1136 health and disease. Amino Acids *37*, 153-168.
1137 Yau, E.H., Kummetha, I.R., Lichinchi, G., Tang, R., Zhang, Y., and Rana, T.M. (2017). Genome-
1138 Wide CRISPR Screen for Essential Cell Growth Mediators in Mutant KRAS Colorectal
1139 Cancers. Cancer Res *77*, 6330-6339.
1140 Ying, H.Q., Kimmelman, A.C., Lyssiotis, C.A., Hua, S.J., Chu, G.C., Fletcher-Sananikone, E.,
1141 Locasale, J.W., Son, J., Zhang, H.L., Coloff, J.L.*, et al.* (2012). Oncogenic Kras
1142 Maintains Pancreatic Tumors through Regulation of Anabolic Glucose Metabolism. Cell
1143 *149*, 656-670.
1144 Yuneva, M.O., Fan, T.W.M., Allen, T.D., Higashi, R.M., Ferraris, D.V., Tsukamoto, T., Mates,
1145 J.M., Alonso, F.J., Wang, C.M., Seo, Y.*, et al.* (2012). The Metabolic Profile of Tumors
1146 Depends on Both the Responsible Genetic Lesion and Tissue Type. Cell Metabolism *15*,
1147 157-170.
1148 Zaytouni, T., Tsai, P.Y., Hitchcock, D.S., DuBois, C.D., Freinkman, E., Lin, L., Morales-
1149 Oyarvide, V., Lenehan, P.J., Wolpin, B.M., Mino-Kenudson, M.*, et al.* (2017). Critical role
1150 for arginase 2 in obesity-associated pancreatic cancer. Nat Commun *8*, 242.
1151 Zhang, Y., Velez-Delgado, A., Mathew, E., Li, D., Mendez, F.M., Flannagan, K., Rhim, A.D.,
1152 Simeone, D.M., Beatty, G.L., and Pasca di Magliano, M. (2017). Myeloid cells are
1153 required for PD-1/PD-L1 checkpoint activation and the establishment of an
1154 immunosuppressive environment in pancreatic cancer. Gut *66*, 124-136.
1155 Zhao, F., Obermann, S., von Wasielewski, R., Haile, L., Manns, M.P., Korangy, F., and Greten,
1156 T.F. (2009). Increase in frequency of myeloid-derived suppressor cells in mice with
1157 spontaneous pancreatic carcinoma. Immunology *128*, 141-149.

1158

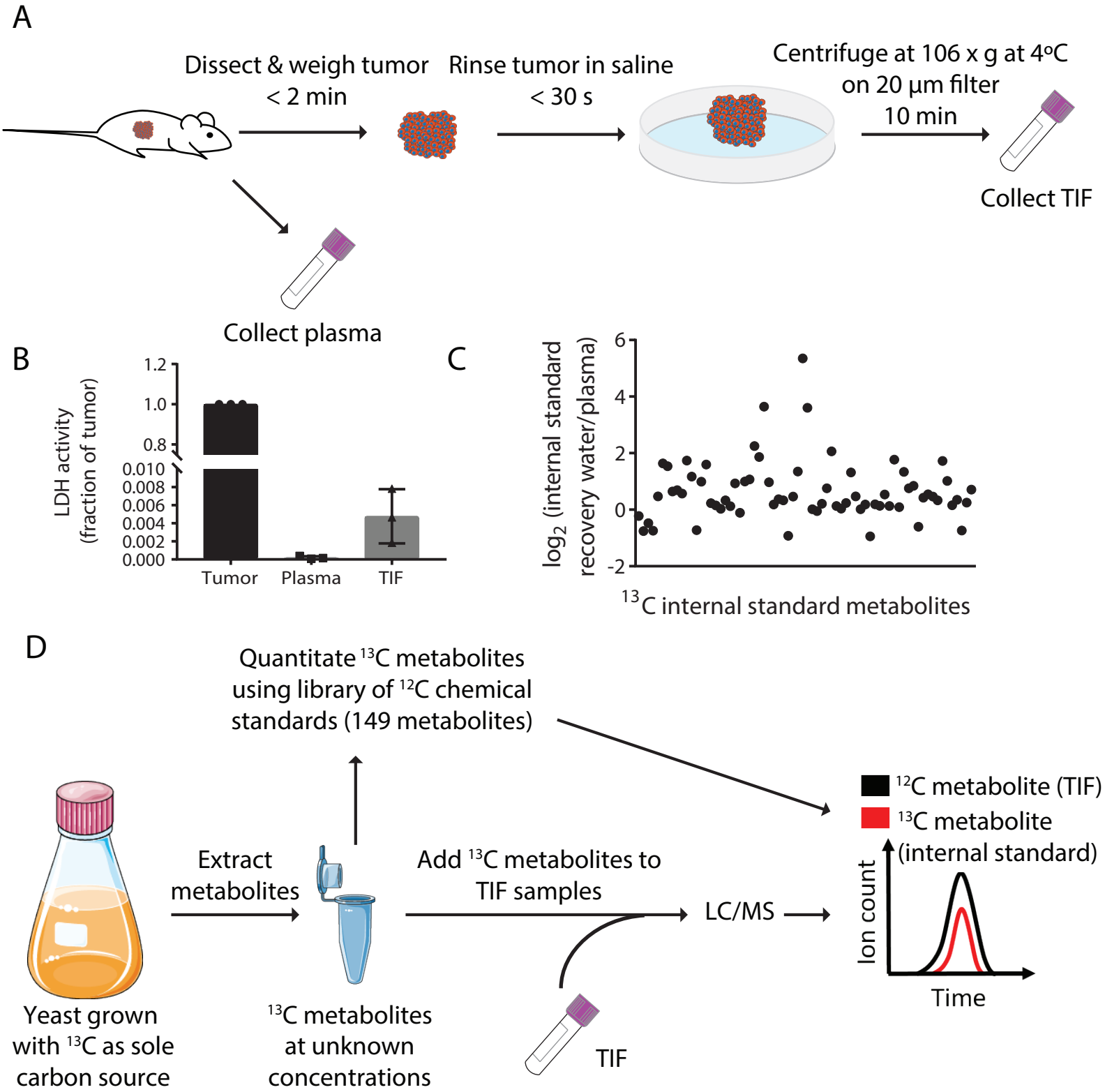
A
Dissect & weigh tumor
< 2 min
Rinse tumor in saline
< 30 s
Centrifuge at 106 x g at 4°C
on 20 µm filter
10 min
Collect TIF
Collect plasma
B
LDH activity
(fraction of tumor)
1.2
1.0
0.8
0.010
0.008
0.006
0.004
0.002
0.000
Tumor
Plasma
TIF
C
log2 (internal standard
recovery water/plasma)
6
4
2
0
-2
13C internal standard metabolites
D
Quantitate 13C metabolites
using library of 12C chemical
standards (149 metabolites)
12C metabolite (TIF)
13C metabolite
(internal standard)
Extract
metabolites
Add 13C metabolites to
TIF samples
LC/MS
Ion count
Time
Yeast grown
with 13C as sole
carbon source
13C metabolites
at unknown
concentrations
TIF

Figure 1

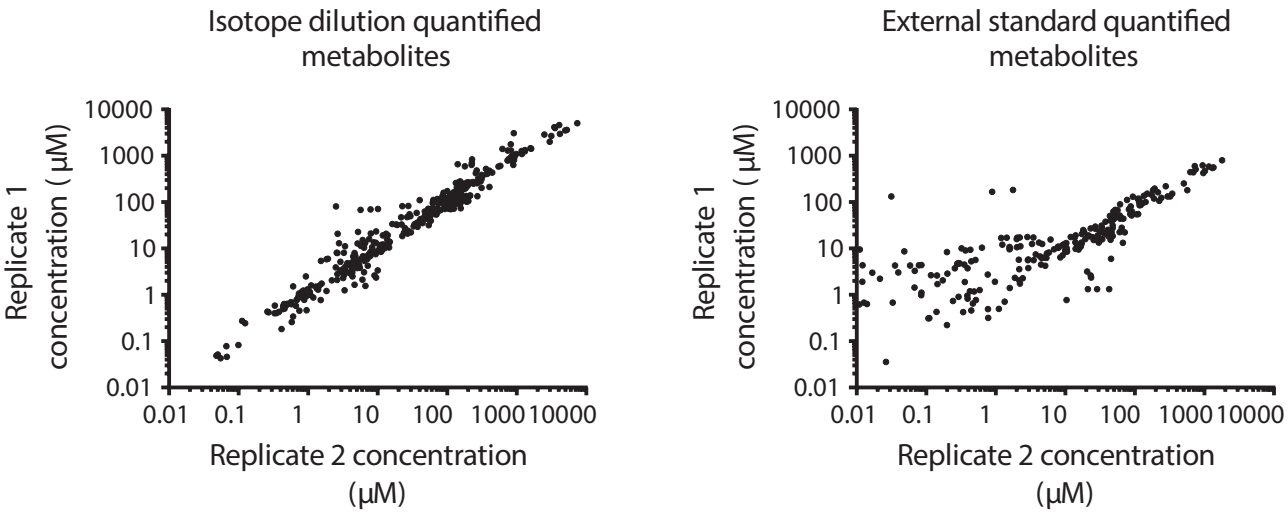

Figure 1 - figure supplement 1

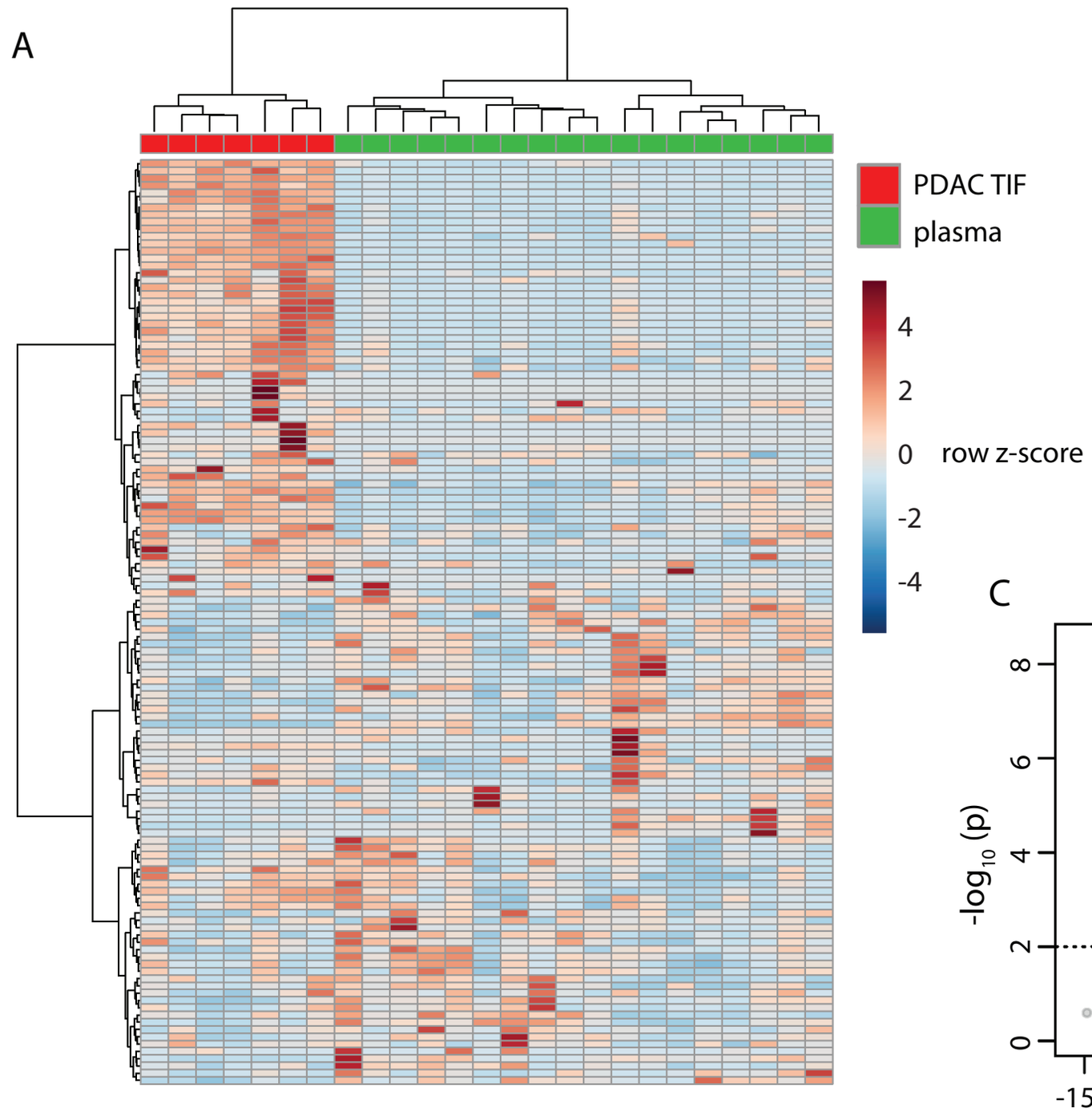
A
PDAC TIF
plasma
4
2
0
-2
-4
row z-score

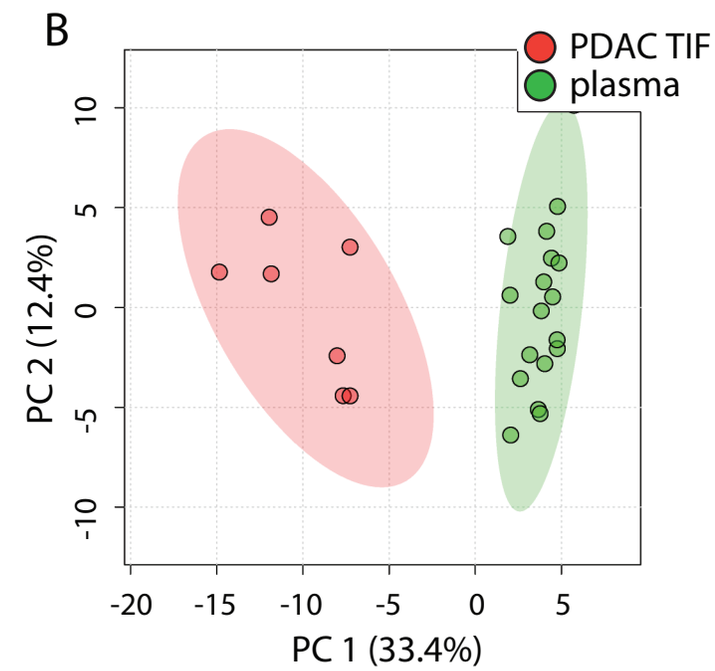
B
PDAC TIF
plasma
PC 2 (12.4%)
PC 1 (33.4%)
10
5
0
-5
-10
-20
-15
-10
-5
0
5

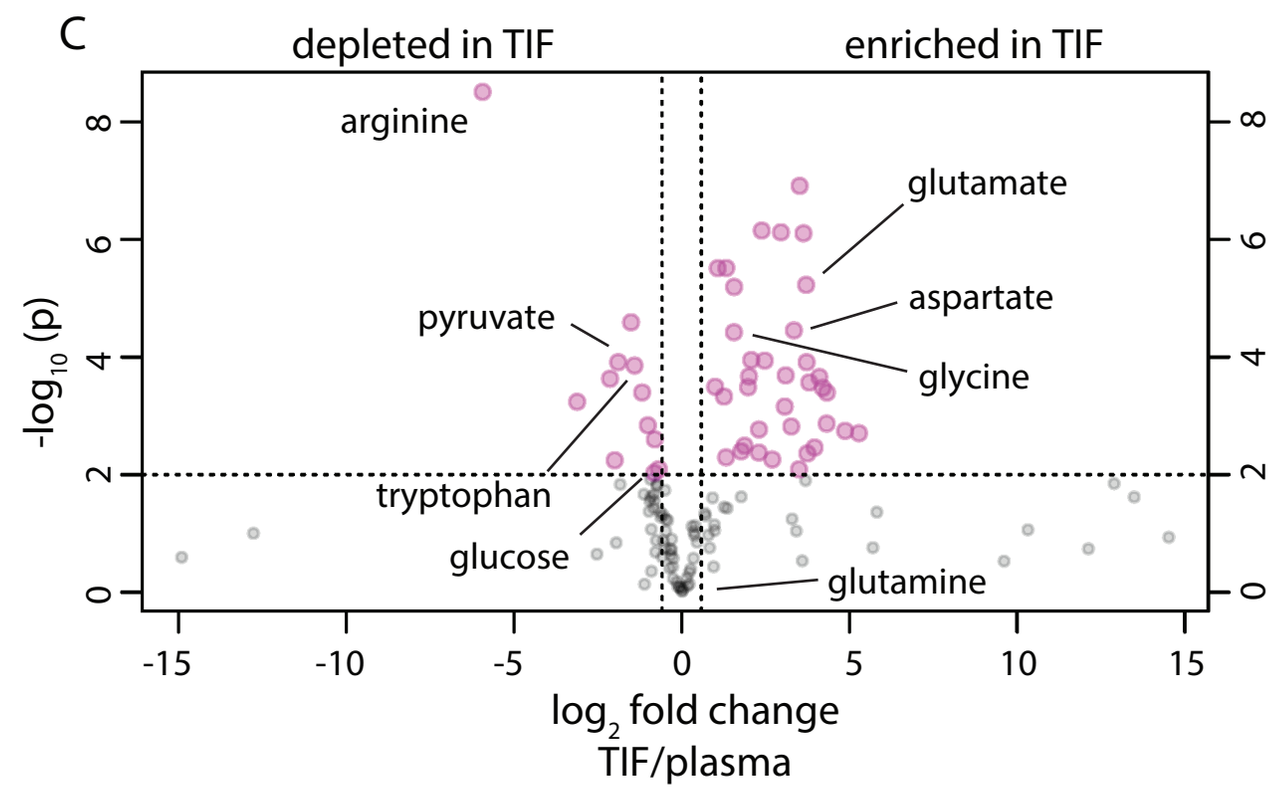
C
depleted in TIF
enriched in TIF
arginine
glutamate
aspartate
pyruvate
glycine
tryptophan
glucose
glutamine
-log10 (p)
log2 fold change
TIF/plasma
-15
-10
-5
0
5
10
15

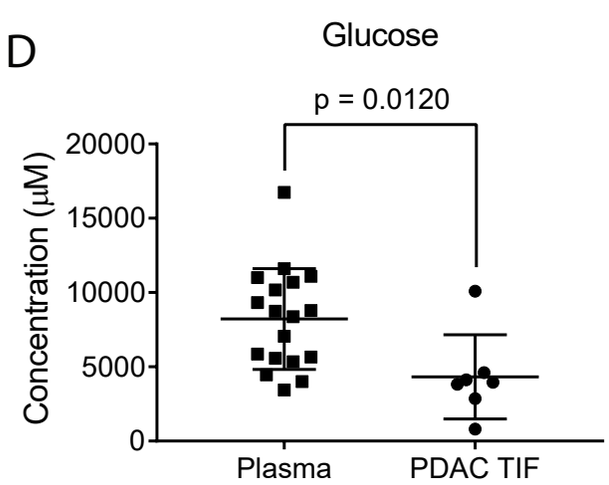
D
Glucose
p = 0.0120
Concentration (μM)
20000
15000
10000
5000
0
Plasma
PDAC TIF

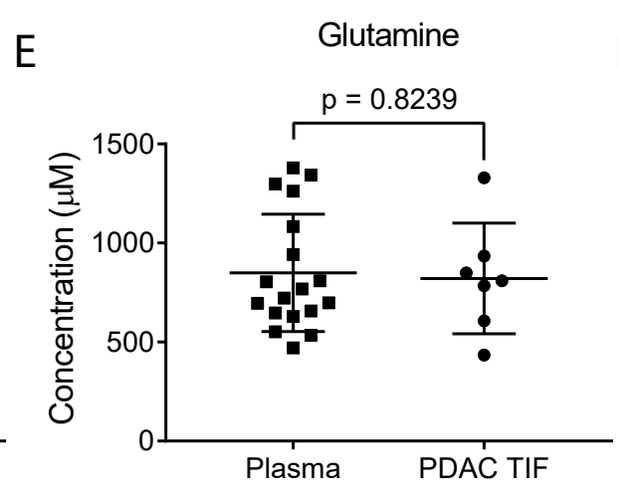
E
Glutamine
p = 0.8239
Concentration (μM)
1500
1000
500
0
Plasma
PDAC TIF

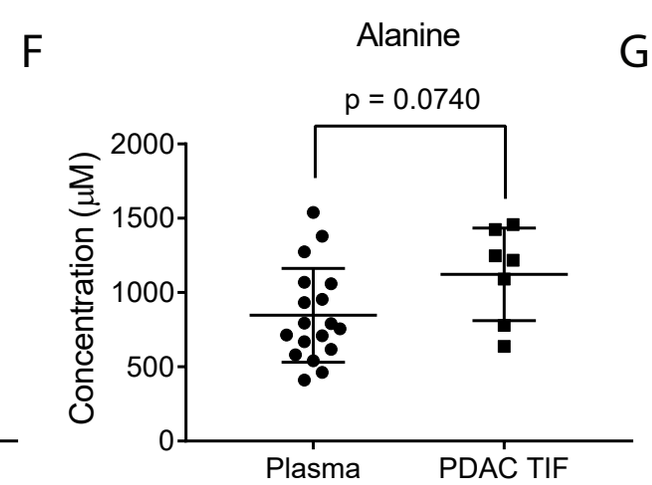
F
Alanine
p = 0.0740
Concentration (μM)
2000
1500
1000
500
0
Plasma
PDAC TIF

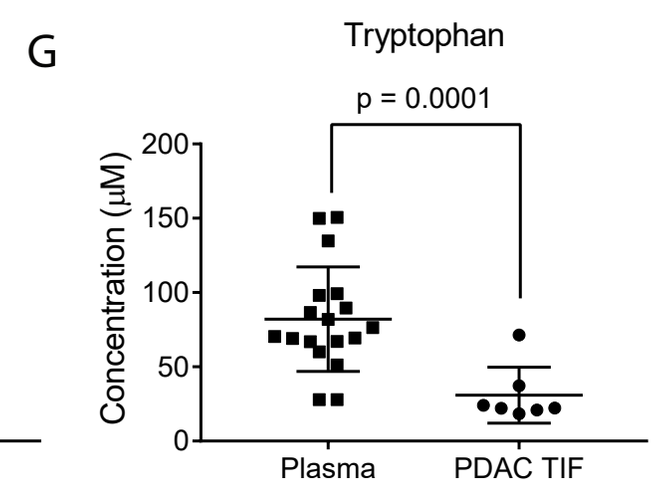
G
Tryptophan
p = 0.0001
Concentration (μM)
200
150
100
50
0
Plasma
PDAC TIF

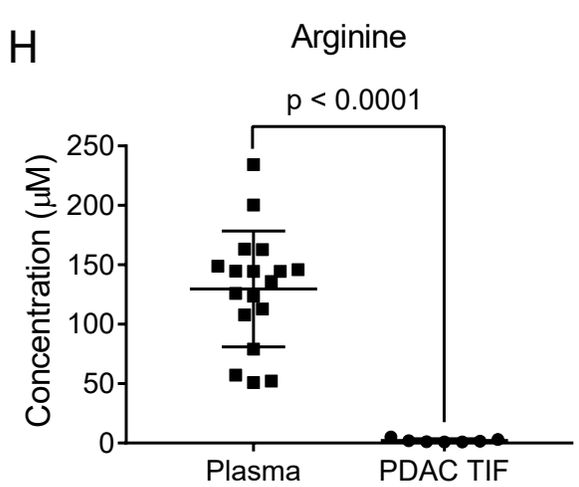
H
Arginine
p < 0.0001
Concentration (μM)
250
200
150
100
50
0
Plasma
PDAC TIF

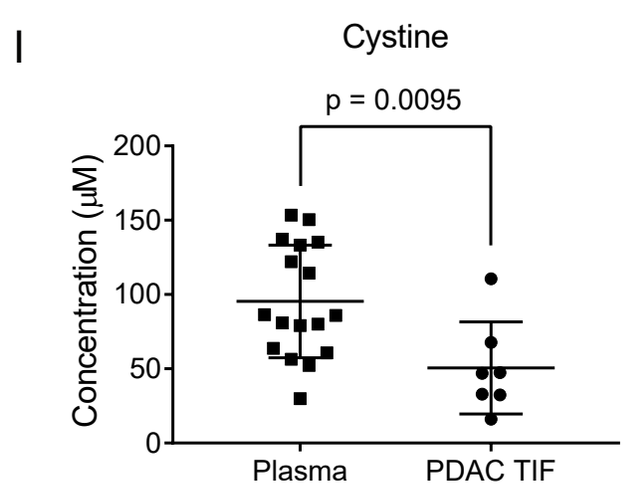
I
Cystine
p = 0.0095
Concentration (μM)
200
150
100
50
0
Plasma
PDAC TIF

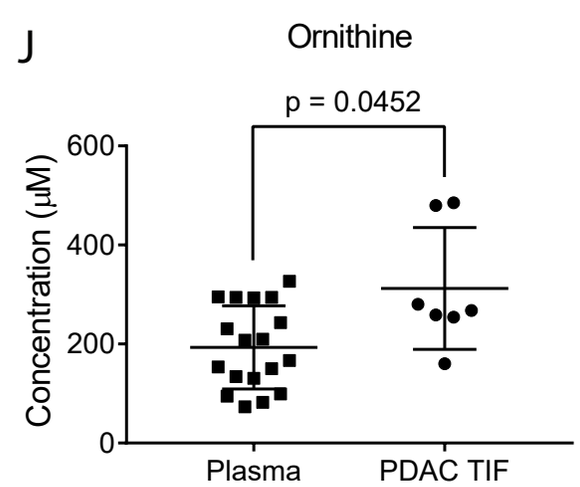
J
Ornithine
p = 0.0452
Concentration (μM)
600
400
200
0
Plasma
PDAC TIF

Figure 2

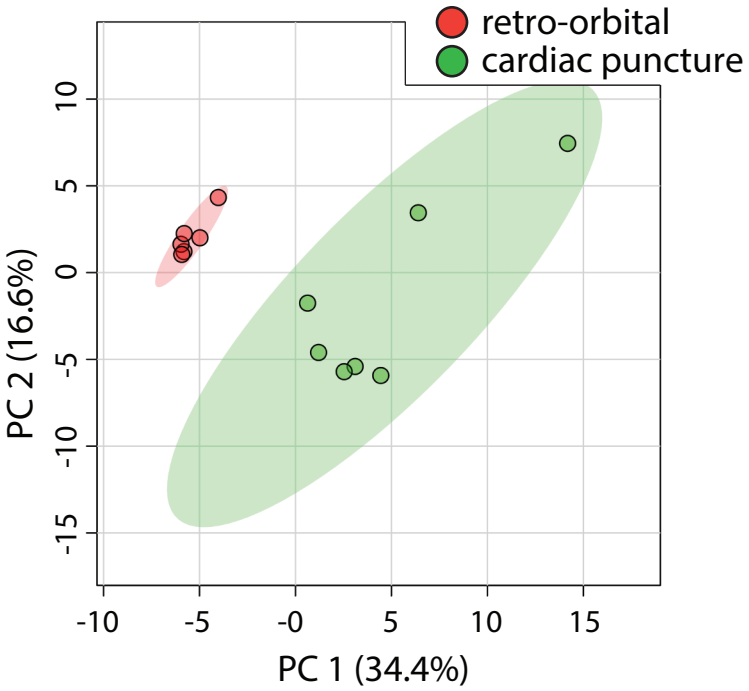

Figure 2 - figure supplement 1

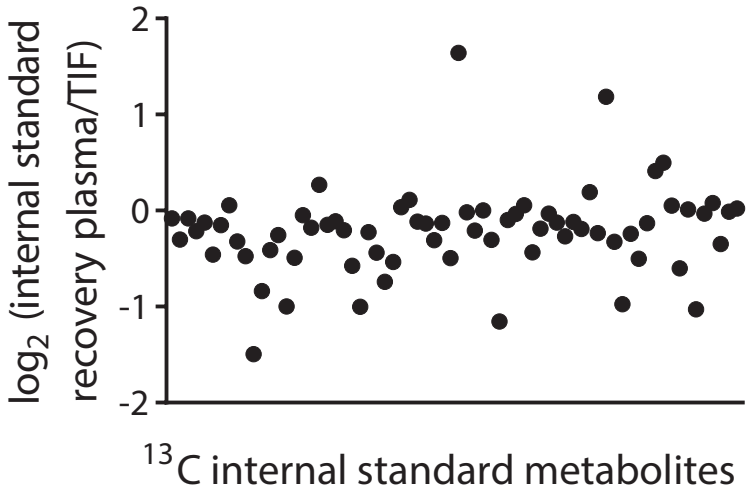

Figure 2 - figure supplement 2

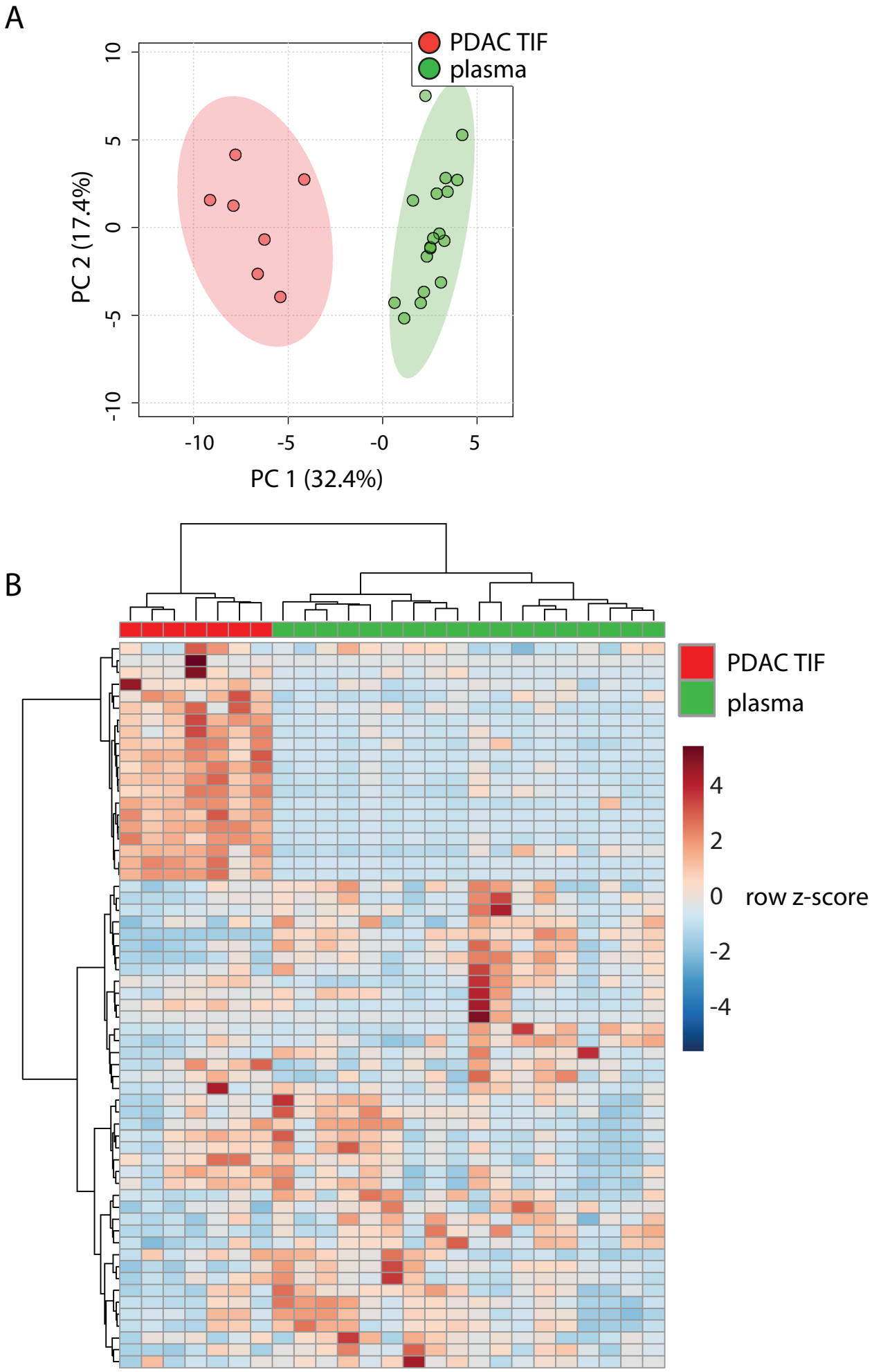

Figure 2 - figure supplement 3

A

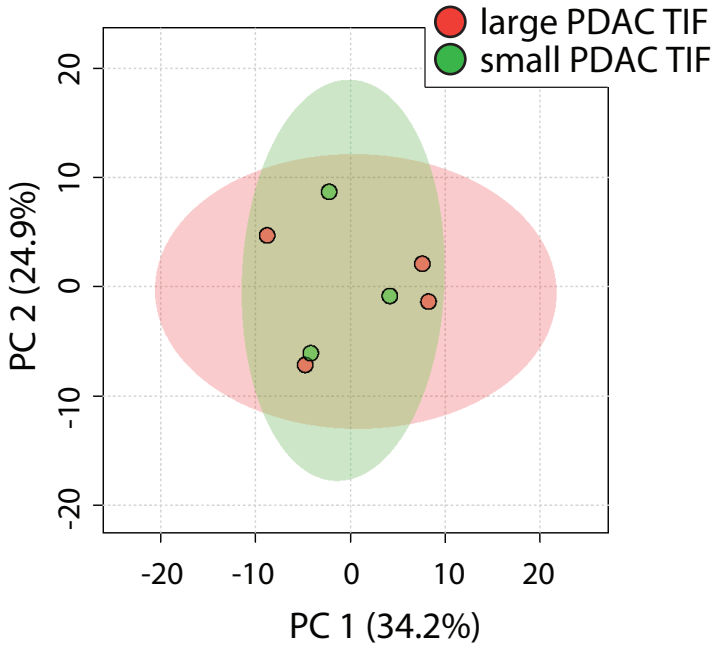

Figure 2 - figure supplement 4

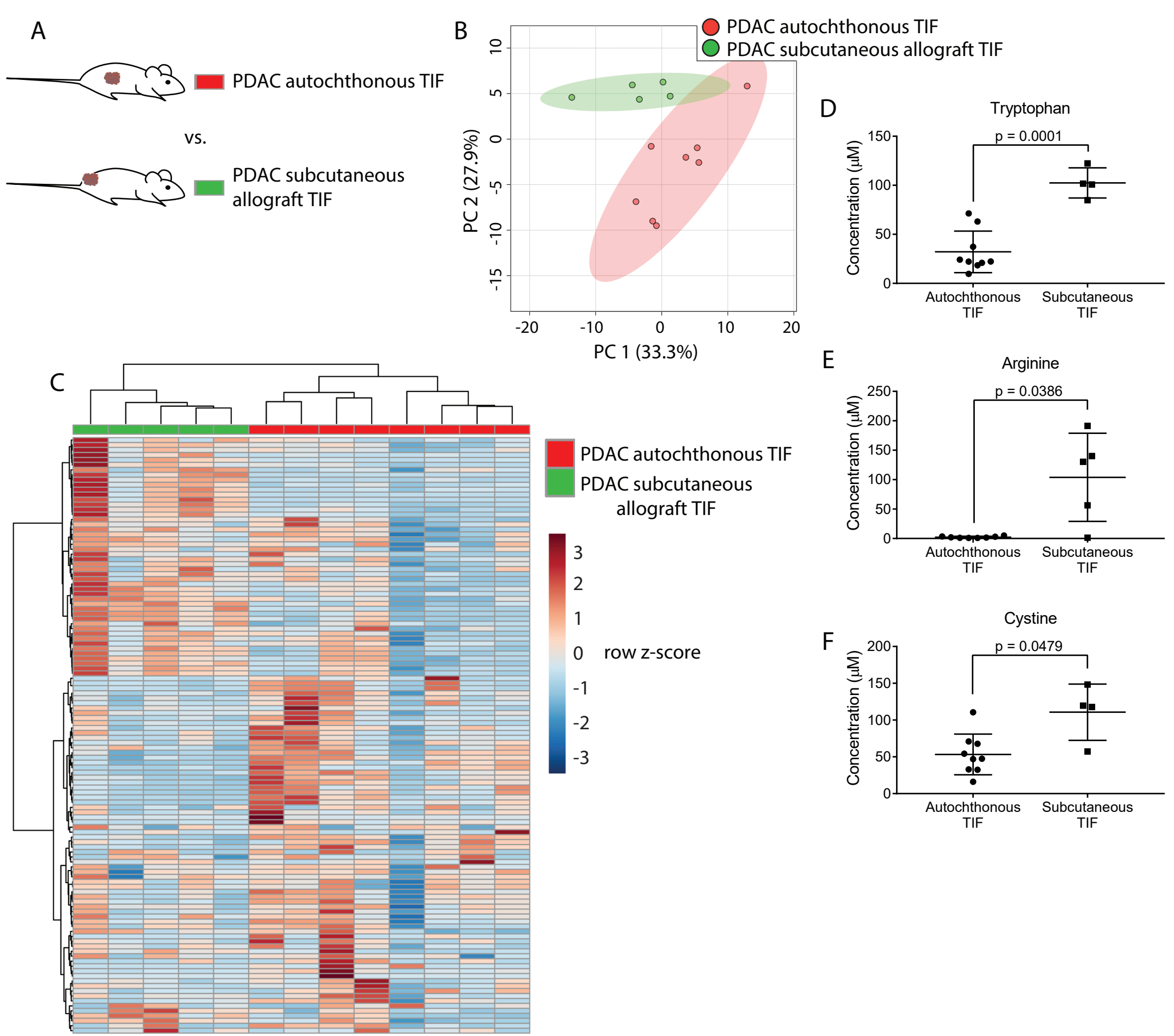
A
PDAC autochthonous TIF
vs.
PDAC subcutaneous allograft TIF
B
PDAC autochthonous TIF
PDAC subcutaneous allograft TIF
PC 2 (27.9%)
PC 1 (33.3%)
C
PDAC autochthonous TIF
PDAC subcutaneous allograft TIF
row z-score
D
Tryptophan
p = 0.0001
Concentration (μM)
Autochthonous TIF
Subcutaneous TIF
E
Arginine
p = 0.0386
Concentration (μM)
Autochthonous TIF
Subcutaneous TIF
F
Cystine
p = 0.0479
Concentration (μM)
Autochthonous TIF
Subcutaneous TIF

Figure 3

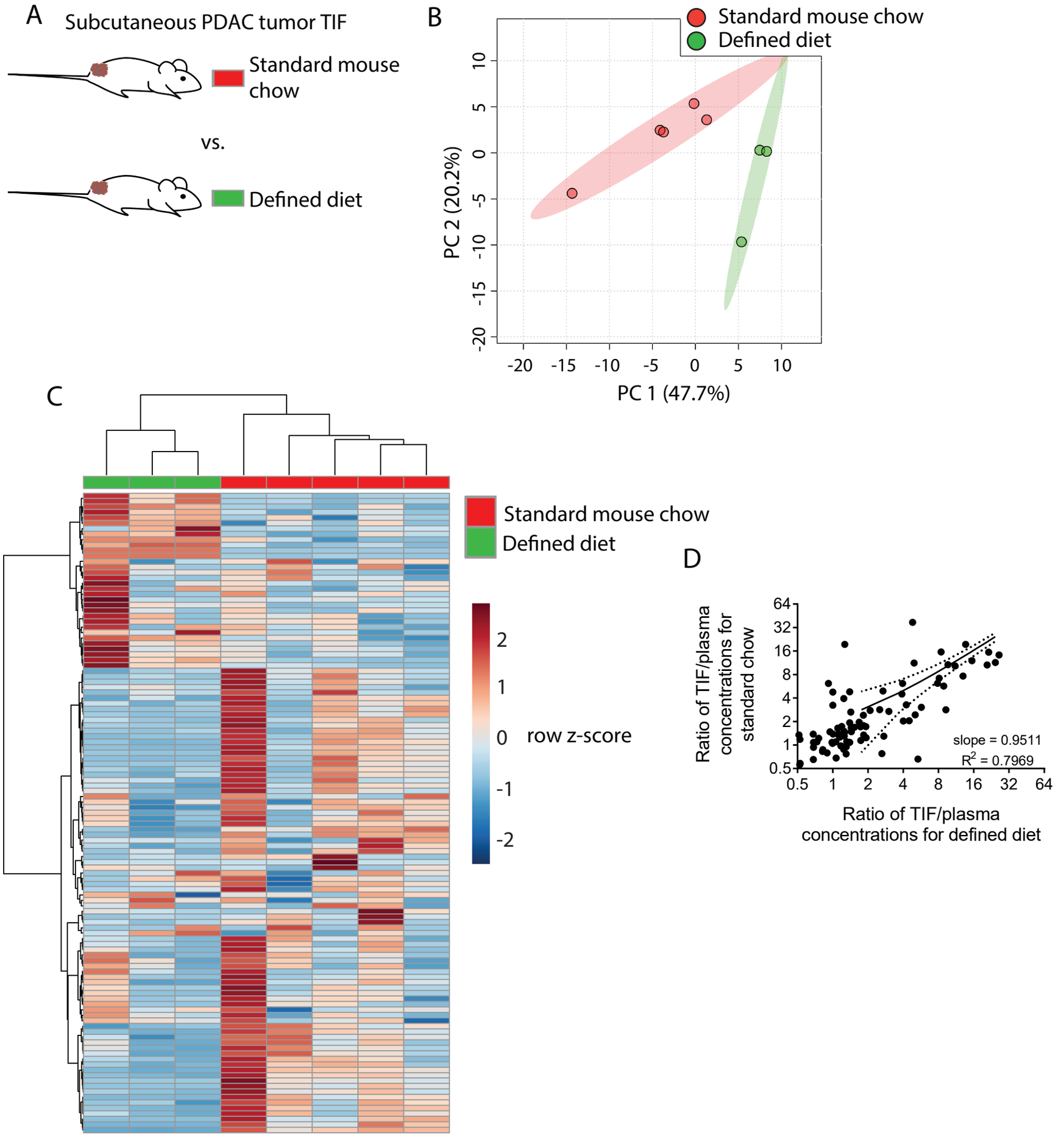
A
Subcutaneous PDAC tumor TIF
Standard mouse chow
vs.
Defined diet
B
Standard mouse chow
Defined diet
PC 2 (20.2%)
PC 1 (47.7%)
C
Standard mouse chow
Defined diet
row z-score
D
Ratio of TIF/plasma concentrations for standard chow
Ratio of TIF/plasma concentrations for defined diet
slope = 0.9511
R2 = 0.7969

Figure 4

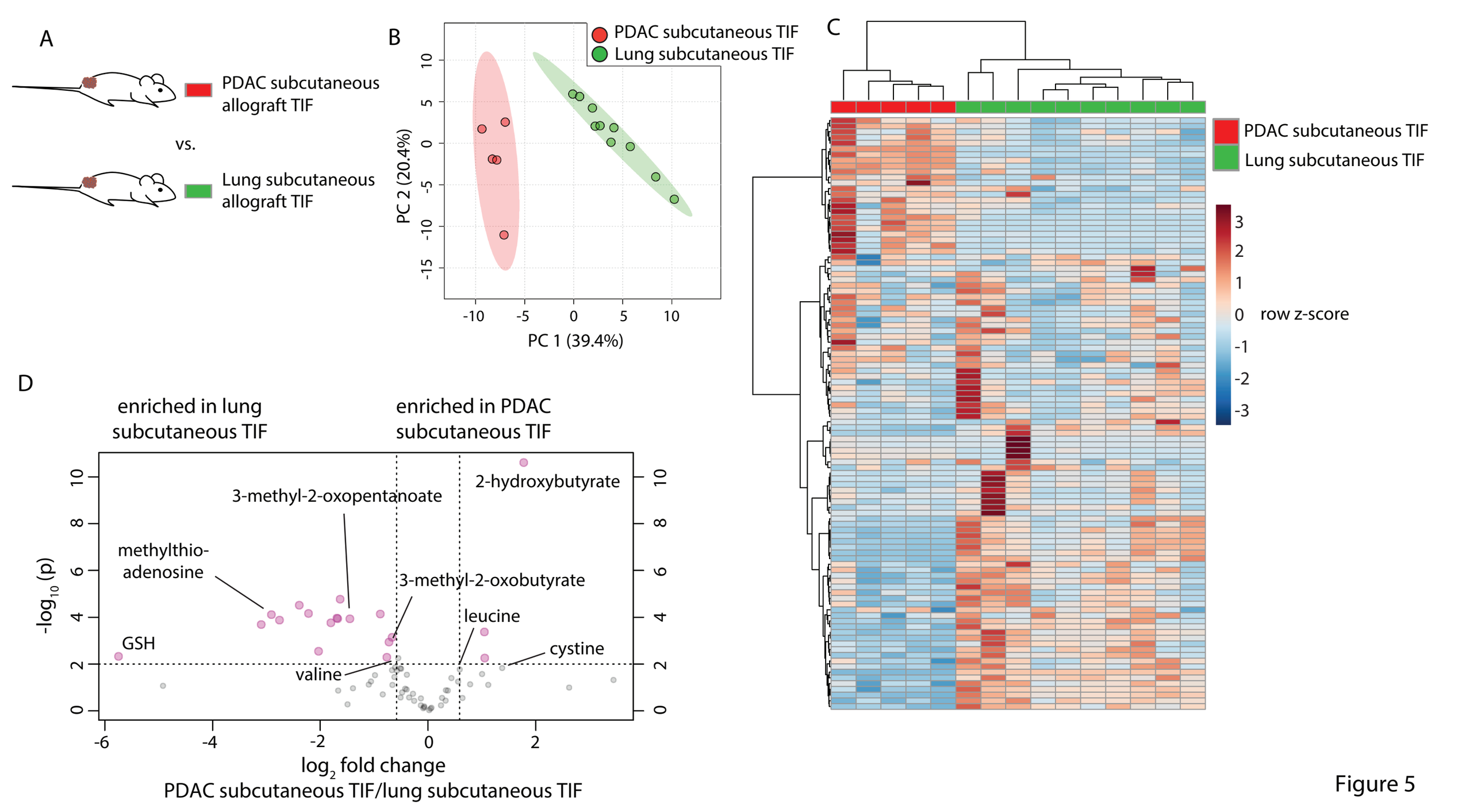
A
PDAC subcutaneous allograft TIF
vs.
Lung subcutaneous allograft TIF
B
PDAC subcutaneous TIF
Lung subcutaneous TIF
PC 2 (20.4%)
PC 1 (39.4%)
C
PDAC subcutaneous TIF
Lung subcutaneous TIF
row z-score
D
enriched in lung subcutaneous TIF
enriched in PDAC subcutaneous TIF
2-hydroxybutyrate
3-methyl-2-oxopentanoate
methylthio-adenosine
3-methyl-2-oxobutyrate
leucine
GSH
cystine
valine
-log10 (p)
log2 fold change
PDAC subcutaneous TIF/lung subcutaneous TIF

Figure 5

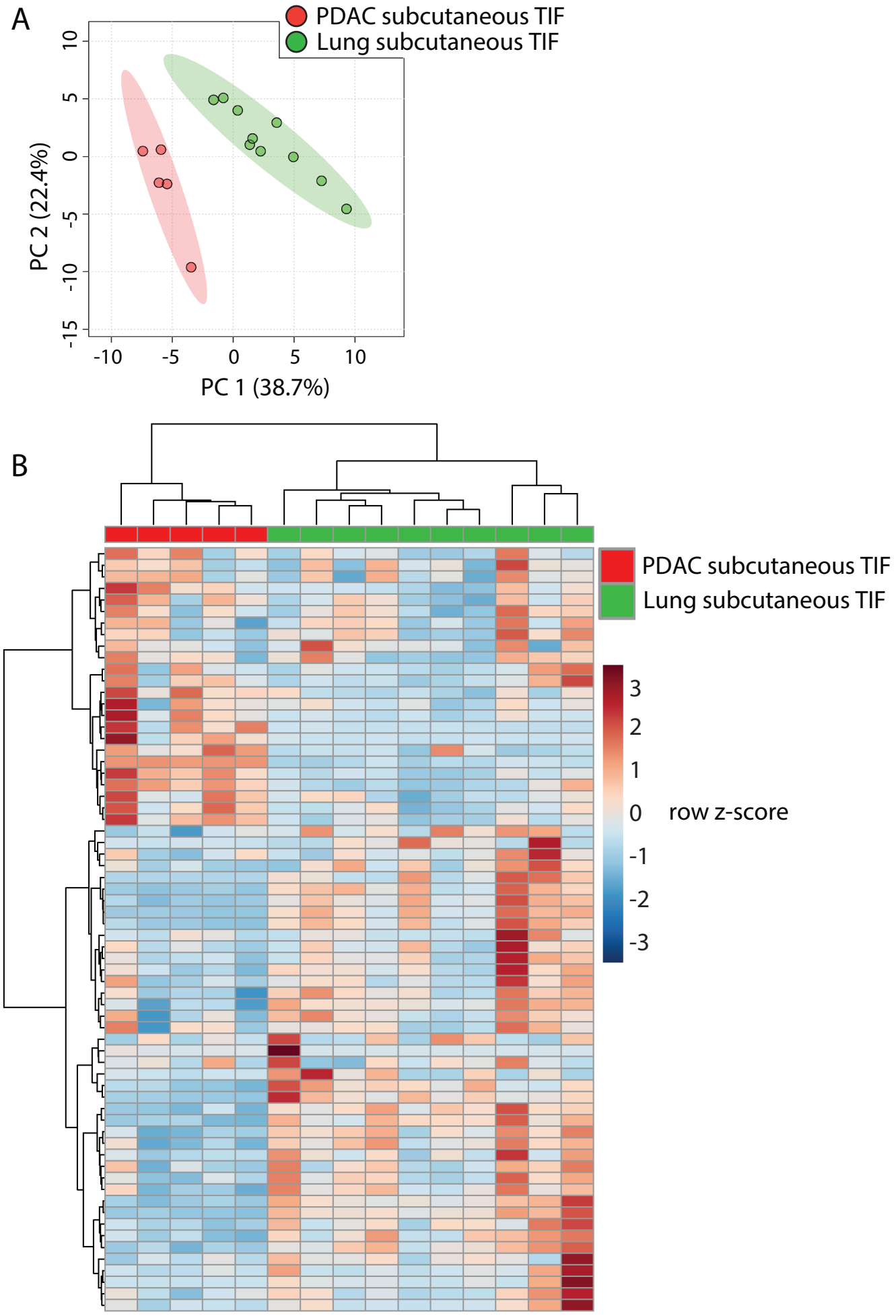

Figure 5 - figure supplement 1

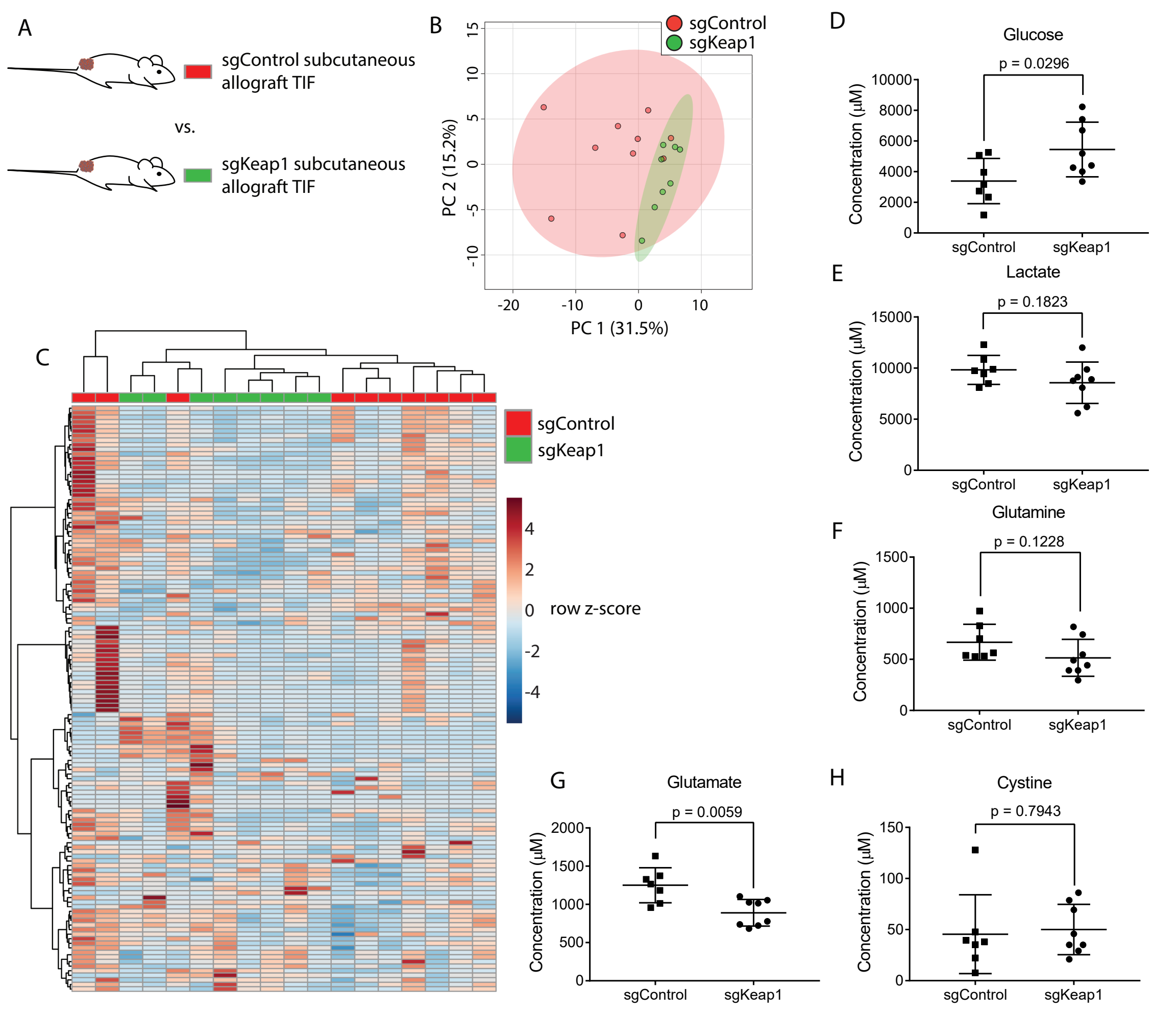
A
sgControl subcutaneous allograft TIF
vs.
sgKeap1 subcutaneous allograft TIF
B
sgControl
sgKeap1
PC 2 (15.2%)
PC 1 (31.5%)
C
sgControl
sgKeap1
row z-score
D
Glucose
p = 0.0296
Concentration (μM)
sgControl
sgKeap1
E
Lactate
p = 0.1823
Concentration (μM)
F
Glutamine
p = 0.1228
Concentration (μM)
G
Glutamate
p = 0.0059
Concentration (μM)
H
Cystine
p = 0.7943
Concentration (μM)

Figure 6